CHAPTER THREE

Dynamical Behavior of Somatostatin-14 and Its Cyclic Analogues as Analyzed in Bulk and on Plasmonic Silver Nanoparticles

Belén Hernández[*,†], Yves-Marie Coïc[‡], Eduardo López-Tobar[§], Santiago Sanchez-Cortes[§], Bruno Baron[¶], Fernando Pflüger[†], Sergei G. Kruglik[‖], Régis Cohen[#], Mahmoud Ghomi[*,†,1]

[*]Laboratoire Matrice Extracellulaire et Dynamique Cellulaire (MEDyC), UMR 7369, Université de Reims, Faculté des Sciences, Reims Cedex 2, France
[†]Groupe de Biophysique Moléculaire, Sorbonne Paris Cité, Université Paris 13, UFR Santé-Médecine-Biologie Humaine, Bobigny, France
[‡]Institut Pasteur, Unité de Chimie des Biomolécules, UMR 3523, Paris Cedex 15, France
[§]Instituto de Estructura de la Materia, IEM-CSIC, Serrano 121, Madrid, Spain
[¶]Institut Pasteur, Plate-Forme de Biophysique de Macromolécules et de leurs Interactions, Paris Cedex 15, France
[‖]Laboratoire Jean-Perrin, Sorbonne Université, UPMC Univ. Paris 06, CNRS UMR 8237, Paris, France
[#]Service d'Endocrinologie, Centre Hospitalier de Saint-Denis, Saint-Denis, France
[1]Corresponding author: e-mail address: mahmoud.ghomi@univ-paris13.fr

Contents

Advances in Protein Chemistry and Structural Biology, Volume 112
ISSN 1876-1623
https://doi.org/10.1016/bs.apcsb.2018.01.002

Abstract

Primarily known as the inhibitor of growth hormone release, the role of somatostatin in many other inhibiting activities upon binding to its five G-protein-coupled receptors has been elucidated. Because of the short half-life of somatostatin, a number of synthetic analogues were elaborated for this peptide hormone. Herein, after recalling the main somatostatin therapeutic interests, we present the dynamical behavior of somatostatin-14 and its two currently used synthetic cyclic analogues, octreotide and pasireotide. Physical techniques, such as fluorescence, UV–visible absorption, circular dichroism, Raman spectroscopy, surface-enhanced Raman spectroscopy, and transmission electron microscopy, were jointly used in order to get information on the solution structural features, as well as on the anchoring sites of the three peptides on silver colloids. While somatostatin-14 adopts a rather unordered chain within the submillimolar concentration range, its cyclic analogues were revealed to be ordered, i.e., stabilized either in a type-II′ β-turn (octreotide) or in a face-to-face γ-turn/type-I β-turn (pasireotide) structure. Nevertheless, a progressive structuring trend was observed in somatostatin-14 upon increasing concentration to the millimolar range. Because of their cationic character, the three peptides have revealed their capability to bind onto negatively charged silver nanoparticles. The high affinity of the peptides toward metallic particles seems to be extremely promising for the elaboration of somatostatin-based functionalized plasmonic nanoparticles that can be used in diagnosis, drug delivery, and therapy.

1. INTRODUCTION

1.1 Therapeutic Interest of Somatostatin and its Analogues

Since its identification in 1973 by Brazeau and Guillemin, somatostatin revealed numerous actions in physiology and pathologies (Brazeau et al., 1973). Many somatostatin analogues (SSAs) have been developed to improve the health status with a high-level evidence-based medicine for patients suffering from benign or malignant neuroendocrine-tumors (NETs) (Caplin et al., 2014; Rinke et al., 2009). Nevertheless, among SSAs, octreotide and lanreotide remain the pivotal therapeutic molecules for controlling hormone-related symptoms of functioning NETs and tumor growth (Modlin, Pavel, Kidd, & Gustafsson, 2010). More recently, another SSA, referred to as pasireotide, having a high affinity to its receptors, extended the therapeutic use to other diseases, i.e., Cushing's disease (McKeage, 2013). Furthermore, in the field of nuclear medicine, the local administration with a high level of radioactivity to treat advanced stages of NETs is rendered possible through the coupling of SSA to an adequate radioisotope (Brabander et al., 2017).

1.1.1 Somatostatin in Physiology

Initially discovered as an inhibitor of growth hormone release, somatostatin is now known to inhibit a variety of gastrointestinal processes. It also affects rates of neurotransmission in the central nervous system. Somatostatin is a peptide hormone, having two active forms with 14 and 28 residues, abbreviated as SST-14 and SST-28, respectively. This hormone is expressed throughout the body and inhibits the release of numerous secondary hormones by binding to high-affinity G-protein-coupled somatostatin receptors, which comprises five distinct subtypes (SSTRi, $i=1, \ldots, 5$). SSTRs express in various regions, such as brain, adrenals, pancreas, and gastrointestinal tract.

1.1.2 SSAs Use in Pathologies

Because of its short half-life (about 2 min) in plasma, the clinical use of somatostatin was limited. SSAs combined with slow-release component were shown to have a much longer half-life that can reach 1 month or more. As somatostatin is able to reduce the portal flow, it has been used for managing bleeding of esophageal varices in patients with liver cirrhosis. It may also suppress pepsin secretion and, hence, alleviate upper gastrointestinal bleeding. In gastroenterology, it is also frequently used to dry intestinal secretions and accelerate the healing of digestive fistulas. In endocrinology, SSAs are indicated to control or decrease numerous hormonal secretions: growth hormone in acromegaly, insulin in insulinomas, ACTH in Cushing's diseases, serotonin in carcinoid syndromes, glucagon, etc.

Antiproliferative action of these components is not only used in the previous endocrine diseases but represents the obligatory passage in the therapeutic courses of the NETs (Mohamed et al., 2014). NETs emerge from neuroendocrine cells of the bronchopulmonary or gastrointestinal system. Their evolutions are slow and indolent with a frequent clinical revelation at metastatic stage. Ninety percent of gastroenteropancreatic (GEP)-NETs express SSTRs on cell surface and may benefit from SSAs-based treatments. Each year an estimated 8000 individuals are newly diagnosed with NET in the United States. When locally advanced or metastatic (70% at diagnosis), with nonfeasible surgery, medical treatments and SSAs should be chosen according to tumor features (Yao et al., 2008).

Two randomized studies evaluated the SSAs efficacy in NETs: CLARINET study (lanreotide) and PROMID trial (octreotide) (Caplin et al., 2014; Rinke et al., 2009). Both proved, vs placebo, a reduction of progression-free survival in well-differentiated metastatic NETs. There

was no difference for overall survival. Meta-analysis confirms that SSAs have an antiproliferative effect in advanced GEP-NETs, reducing disease progression risk by 41%, with a good safety (Merola, Panzuto, & Delle Fave, 2017).

1.1.3 Radiolabeled SSAs in Imaging and Therapy

The overexpression of SSTRs is a characteristic of NETs and can be used to localize the primary tumor or its metastases by imaging with the radiolabeled SSAs (Table 1). The majority of tumors expressed SSTR2, and also SSTR1, SSTR3, and SSTR5, and a minority expressed SSTR4 (Reubi, Waser, Schaer, & Laissue, 2001). SSTR imaging is necessary for staging, therapy planning, and follow-up. Imaging with radiolabeled SSAs has high specificity, low antigenicity, rapid clearance, and good tissue distribution. Initially Octreoscan™ was the only radiopharmaceutical binding to SSTR2. Because of some limits in precision, other components labeled with Gallium 68 combined with PET scan technology were used. In the PET diagnostics, there are three routine SSA tracers labeled with ^{68}Ga: DOTA-TATE, DOTA-TOC, and DOTA-NOC. All three tracers bind specifically with SSTRs. ^{68}Ga-labeled SSTRs have high sensitivity (82%–97%) and specificity (80%–92%) in the detection of small primary tumors or metastases of NETs (Barrio et al., 2017; Wang et al., 2013).

Table 1 Overview of Radiolabeled Somatostatin Analogues (SSAs) and Their Uses in Medicine

Theranostic Molecule	Somatostatin Analogue (SSA)
Target	SSTRs, especially SSTR2
Planar imaging	SSA labeled with indium-III
SPECT or PET	[^{68}Ga]Ga-DOTA-TATE
	[^{68}Ga]Ga-DOTA-TOC
	[^{68}Ga]Ga-DOTA-NOC
Therapeutic agent	[^{177}Lu]Ga-DOTA-TATE
	[^{177}Lu]Ga-DOTA-TOC
	[^{90}Y]Ga-DOTA-TOC
	[^{90}Y]Ga-DOTA-TATE
Indication	NETs

High level of radioactivity delivered locally can be used to destroy tumoral cells. Peptide receptor radionuclide therapy (PRRT) is a systemic therapy in patients with advanced metastatic NET. PRRT requires a good tumor uptake in the SSTR imaging. For therapeutic purposes, the peptides DOTA-TATE and DOTA-TOC can be labeled with either ^{90}Y or ^{177}Lu. PRRT has yielded very promising results in selected patients (Table 1). It produces good tumor response rates with limited and reversible side effects (Brabander et al., 2017).

1.1.4 SSA Perspectives in Humans

New imaging technology, modification of SSA structure, and binding to other components are the ways of future development of these analogues. Technology of imaging has been improved in recent years by the capacity of detection and better localization of signal in body by multibarret-computerized tomography and magnetic resonance imaging. After static imaging, it is possible to perform functional imaging with an improvement in diagnostic performance of PET–CT imaging of NETs. New radiolabeled ligands and SSAs are in development and could be, in the future, the keys of a more personalized localization and therapy of these tumors (Chatalic, Kwekkeboom, & de Jong, 2015). A functionalized nanoparticle (NP) incorporated with SSAs could modify the targeting, through a preferential binding to cancer cells (Shekhter Zahavi et al., 2017).

1.2 Background Structural Data of SST-14, Octreotide, and Pasireotide

Since the first years following the discovery of SST-14, attempts have rapidly grown up to elucidate the structure–activity relationship of this peptide hormone. It was shown that the presence of the Trp^8-Lys^9 pair of central residues (Fig. 1A) plays a key role in the interaction of SST-14 with SSTRs (Weckbecker et al., 2003). Upon this consideration, it was first thought that SST-14 might have a β-hairpin structure with Trp^8 as the top turn residue. Strikingly, despite the absence of any evident β-sheet marker, the circular dichroism (CD) signal observed in the 100–160 μM concentration range was assigned to a rigid β-turn (Holladay & Puett, 1976; Holladay, Rivier, & Puett, 1977). Later, on the basis of nuclear magnetic resonance (NMR) data obtained in the millimolar (mM) concentration range, it has been concluded that SST-14 cannot adopt a unique rigid structure, but rather fluctuates among several rapidly interconverting conformers, forming somehow a wave-like motion between Cys^3 and Cys^{14} residues

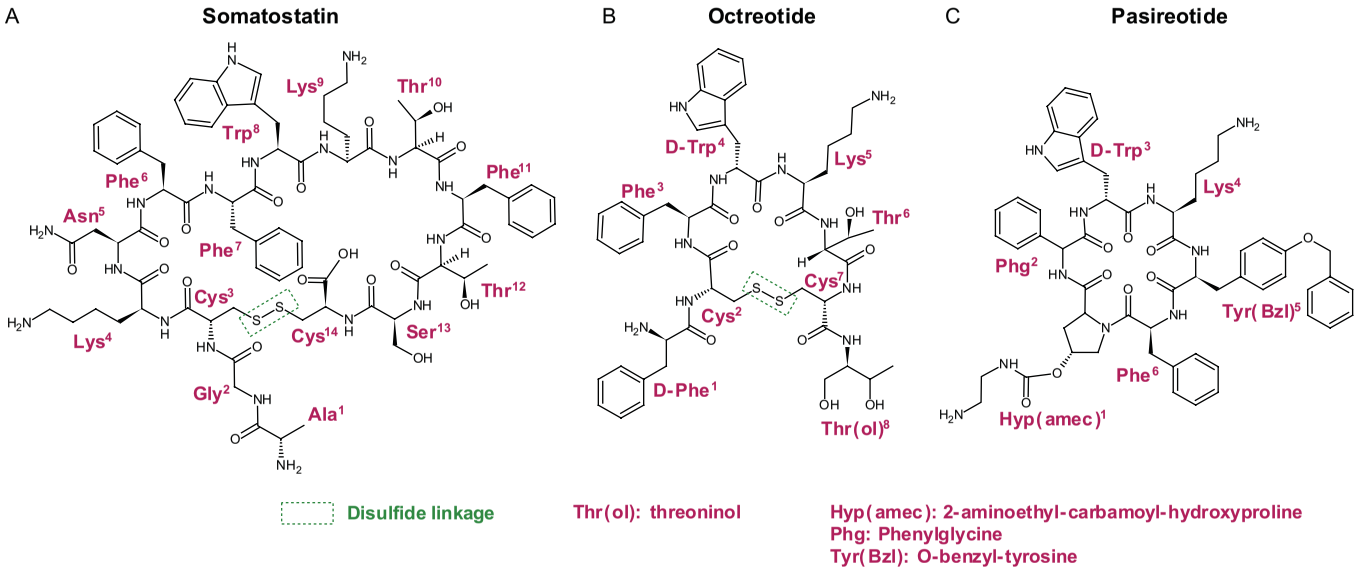

Fig. 1 Chemical composition and amino acid numbering of somatostatin-14 (A), octreotide (B), and pasireotide (C).

(Hallenga et al., 1979, 1980; Knappenberg et al., 1982), In addition, the severe NMR line broadening observed above 15 mM was correlated to the SST-14 aggregation in solution (Hallenga et al., 1980).

The chemical composition of octreotide is closely related to that of SST-14 (Fig. 1B). It should be emphasized that the biological activity of a cyclic SST-14 was shown to be considerably enhanced by the L–D substitution of the central Trp residue (Brown, Rivier, & Vale, 1976; Vale, Grant, Amoss, Blackwell, & Guillemin, 1972). Two D-stereoisomers (D-Phe^{1} and D-Trp^{4}), as well as a C^{ter}-threoninol, Thr^{8}(ol), were introduced in this SSA. Octreotide is the only SSA for which the crystal structure is available (Pohl et al., 1995). It was shown that three molecules (referred to as I, II, and III) surrounded by water were present in the crystal asymmetric unit. All three molecules have a type-II′ β-turn structure formed around the central D-Trp^{4}-Lys^{5} pair. It should be stressed that β-hairpins are the most occurring structural elements in proteins, allowing connection between helices and β-sheets. A β-turn is composed of four residues, generally referred to as i, $i+1$, $i+2$, and $i+3$, and the folding through a β-turn is made possible by the special values given to the backbone torsion angles (ϕ and ψ) of the two middle $i+1$, $i+2$ residues. On the other hand, the so-called reverse β-turns (named type-I′ and -II′) were recognized to be the most frequent ones (Das, Naganagowda, Karle, & Balaram, 2001; Sibanda & Thornton, 1985). Particularly, a type-II′ β-turn is generally formed with a backbone ϕ_{i+1} value close to +60°, limiting the choice of the amino acid type placed at the $i+1$ position (Gunasekaran, Ramakrishnan, & Balaram, 1997; Kaur & Raghava, 2004). In octreotide, three possible reasons might explain the formation of a type-II′ β-turn: (i) the presence of the D-Trp^{4} residue at the turn $i+2$ position, (ii) the shortness of the cyclic part (6 residues instead of 12 in SST-14), (iii) and the presence of a disulfide bridge closing the β-hairpin. Following the analysis of the octreotide crystal structure, ^{1}H NMR data collected from this peptide in DMSO-d_6 also revealed the presence of two major conformers stabilized by a type-II′ β-turn structure (Melacini, Zhu, & Goodman, 1997).

In contrast to SST-14 and octreotide, the peptide bonds are responsible for maintaining the pasireotide cyclic structure (Fig. 1C). As a consequence, the definition of the N^{ter}–C^{ter} course along the pasireotide backbone is not evident. In this report, we have adopted the same amino acid numbering as that suggested previously (Interlandi, 2009). As in the case of octreotide, pasireotide contains a D-Trp^{3}-Lys^{4} neighboring pair. The presence of three synthetic amino acids, i.e., Hyp(amec)^{1}, Phg^{2}, and Tyr(Bzl)^{5}, is to be

remarked in this SSA. Very limited structural data were available for pasireotide. Only a set of NMR-based molecular dynamics (MD) data had conducted to the conclusion that octreotide and pasireotide might have similar structural features, fluctuating between a flat and a saddle-like backbone configuration (Interlandi, 2009; Lewis et al., 2004).

1.3 Plasmonic NPs Used in Biology and Medicine

The main interest of NPs in material science is related to their exceptionally large surface/volume (s/v) ratio. To give a typical example, spherical objects provide an s/v ratio as: $6/D$, where D is their size (diameter). At the nanometric scale, this ratio varies in the decreasing order: 1.2, 0.12, and $0.04\,\mathrm{nm}^{-1}$, for the increasing D values: 5, 50, and 150 nm, respectively. For comparison, the s/v ratio of a ping-pong ball ($D \sim 4$ cm) is as low as $\sim 1.5 \times 10^{-7}\ \mathrm{nm}^{-1}$.

The NPs' remarkable physicochemical properties, different from those encountered in the bulk, correspond to their catalytic activity, magnetism, thermal and electric conductivity, melting point, optical absorption, and scattering.

The use of different types of NPs has gained a continuously increasing attention in biological and medical applications. For instance, we can mention: (i) the organic NPs made of NIPAM/BAM copolymer used for accelerating the aggregation of human β2-microglobulin protein (Linse et al., 2007); (ii) the inorganic NPs, such as those elaborated either from CdTe employed for preventing the fibrillation (Yoo et al., 2011), or those made by uniform maghemite γ-Fe_2O_3 for accelerating/inhibiting the fibrillation of amyloid β (Aβ) peptides involved in Alzheimer's disease (Skaat, Shafir, & Margel, 2011); and (iii) the metallic gold NPs that have shown a large spectrum of action including the inhibition of the aggregation of short size Aβ peptides (Ma, Wei, & Yang, 2013), the acceleration of fibrillation of cysteine-free peptides (Nergiz, Slocik, Naik, & Singamaneni, 2013), as well as the retardation of insulin fibrillogenesis process (Hsieh, Chang, & Cho, 2013).

Focusing particularly on plasmonic NPs, made currently of noble metals (typically Au, Ag, Pt, and Cu) characterized by a high reflectivity, their remarkable optical properties have received a great attention. This type of NPs exhibits strong UV–visible absorption bands that are not present in bulk metal, proving their solution brilliant colors. When a metallic NP is exposed to an electromagnetic wave, the electrons at the surface of the metal (surface

plasmon or SP) oscillate at the same frequency as the incident wave. Then the oscillating electrons reradiate electromagnetic wave at the same frequency. Particularly, upon irradiation with a wavelength (λ) that matches the principal plasmon absorption (λ_p), giving rise to the so-called surface plasmonic resonance (SPR), the NPs can absorb and scatter the light beam out of their physical cross sections (Aslan, Lakowicz, & Geddes, 2005; Hutter & Fendler, 2004). It has been evidenced that the absorption maxima of the SP band depends on the metal type, as well as on the size and shape of the nanostructures. Furthermore, the electric field of the scattered light is highly enhanced when the size of NPs is comparable to or smaller than the wavelength of the light exciting the surface plasmons. This phenomenon, referred to as localized surface plasmon resonance (LSPR), is greatly sensitive to the refractive index. As a consequence, the change in refractive index by the adsorption of biological molecules on the plasmonic NPs surface results in a large redshift of λ_p.

The elaboration of colloidal plasmonic NPs, particularly those made of Au and Ag, was described during the last years (Agnihotri, Mukherji, & Mukherji, 2014; Bastús, Comenge, & Puntes, 2011; Liz-Marzán, 2004; Sanchez-Cortes, Garcia-Ramos, Morcillo, & Tinti, 1995; Shenashen, El-Safty, & Elshehy, 2013), along with the synthesis protocols that give rise to a variety of nanoshapes, such as nanospheres, nanowires, nanorods, nanocubes, nanoflowers, dendrites, nanoprisms, nanoplates, and nanodisks. In parallel, the influence of the shape and size of gold nanoparticles (AuNPs) in exploring biological systems has been reported (Lee & El-Sayed, 2006; Li, Jing, Zhang, & Long, 2012; Paige Hall et al., 2008). As far as the pharmaceutical and medical applications of plasmonic NPs are concerned, one can remark an intensive research performed in drug delivery (Abdellatif et al., 2016), cancer and photothermal therapy (Huang, El-Sayed, Qian, & El-Sayed, 2006; Jain, El-Sayed, & El-Sayed, 2007; Qian, Cao, & Long, 2016), and other diseases (Karimi et al., 2016; Kharlamov et al., 2015).

In the field of biomolecular spectroscopy, benefit was taken from the LSPR effect for analyzing the molecules adsorbed on the surface of plasmonic NPs. Especially, in the two spectroscopic methods, i.e., surface-enhanced fluorescence (SEF) and surface-enhanced Raman scattering (SERS), plasmonic NPs were employed in order to obtain electronic and vibrational information on the biomolecules in the vicinity of plasmonic NPs (Sevilla et al., 2012). Because of a considerable amplification of both incident and scattered light beams, SERS permits detection of very low traces of biological molecules in solution; it can also be used as a tool for

probing the binding sites of the adsorbed species by means of the vibrational markers (Hernández et al., 2016; López-Tobar et al., 2015).

2. RESULTS AND DISCUSSION

2.1 Bulk Structural Dynamics of SST-14 and Its Analogues

2.1.1 Rotational Freedom of the Trp Residue Evidenced by Fluorescence Data

The normalized emission spectra of SST-14 (Fig. 2A), octreotide (Fig. 2B), and pasireotide (Fig. 2C), obtained by excitation at 290 nm, reveal the fluorescence signal of the unique Trp residue involved in these peptides. A large band is observed at ~350 nm, barely affected by increasing the solution ionic strength (Fig. 2). Nevertheless, in low dielectric constant solvents, such as water/methanol mixture or methanol, the Trp fluorescence of SST-14 undergoes a considerable decrease (between 25% and 50%) along with a 10–15 nm downshift (Hernández et al., 2014). The same behavior was observed in octreotide and pasireotide (Hernández et al., 2016). A similar effect had also been revealed on SST-14 interacting with lipids (Beschiaschvilli & Seeling, 1991; Bhattacharyya & Basak, 1995). The values of anisotropy ratio, $\langle r \rangle$, as derived from the linearly polarized emission spectra of SST-14, octreotide, and pasireotide, are reported in Table 2. Being close to zero, these values are consistent with a high rotational freedom of the Trp residue.

2.1.2 CD Structural Fingerprints

In contrast to their fluorescence spectra, the CD spectra of the three peptides present completely different shapes. The SST-14 dichroic spectrum (Fig. 3A) is characterized by a deep minimum at ~203 nm, remaining unchanged in the 100–500 μM concentration range (Hernández, Carelli, Coïc, De Conninck, & Ghomi, 2009). This signal also remains unchanged by increasing ionic strength (Fig. 3A) or by dissolving the peptide in methanol (Hernández et al., 2009). The whole set of observed data shows that in the submillimolar concentration range, SST-14 adopts a rather unordered chain. We recall that a random chain is characterized by a deep negative signal at ~198 nm (Perczel & Fasman, 1992). In a previous study, it is shown that an open-chain SST-14 (in which Cys^3 and Cys^{14} are replaced by Ser residues) provides the same spectral shape in water as the cyclic SST-14, leading us to conclude that the disulfide linkage has no essential effect on the peptide hormone folding. However, the open-chain SST-14 was shown to adopt a helical conformation in methanol (Hernández et al., 2009).

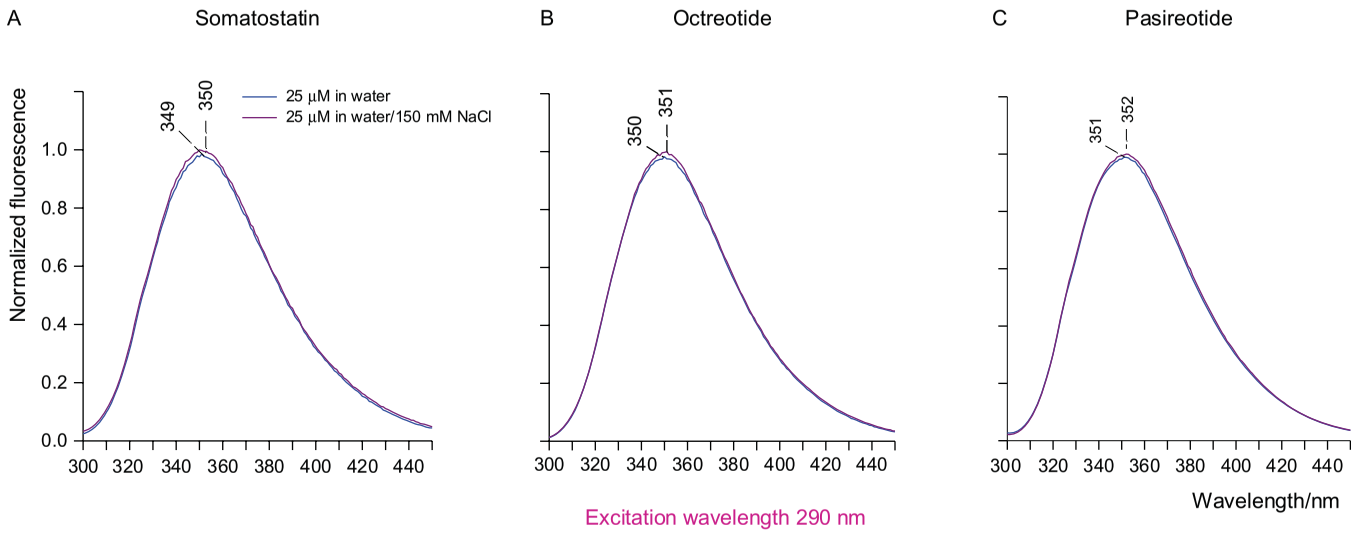

Fig. 2 Normalized fluorescence spectra of somatostatin-14 (A), octreotide (B), and pasireotide (C) obtained by excitation at 290 nm. See Table 2 for anisotropy values.

Table 2 Fluorescence Anisotropy Values, $\langle r \rangle$ Measured in Aqueous Solution[a,b]

	Pure Water	Water/150 mM NaCl
Somatostatin-14	0.022	0.022
Octreotide	0.001	0.001
Pasireotide	0.016	0.001

[a]Each value corresponds to the average of 60 measurements.
[b]Identical anisotropy values were obtained for the three excitation wavelengths at 275, 290, and 295 nm.

The CD spectral shape of octreotide (Fig. 3B) is mainly composed of two negative bands at ~200 and ~217 nm, followed by a large positive band between 240 and 270 nm. In contrast to SST-14, a concentration effect can be observed in the 25–250 μM range, as characterized by a progressive wavelength upshift of the double minima, and a change in its intensity ratio, i.e., $[\Phi_2]/[\Phi_1]$, where $[\Phi_2]$ and $[\Phi_1]$ refer to the ellipticities of the higher and lower wavelength components of the doublet, respectively. CD and NMR-based structural studies on 10 gramicidin S cyclic peptides, all adopting a type-II′ β-turn, revealed that the $[\Phi_2]/[\Phi_1]$ ratio can be taken as an indicator of their hairpin stability (Gibbs, Bjorndahi, Hodges, & Wishart, 2002). Precisely, for a highly stable (compact) β-turn, the $[\Phi_2]/[\Phi_1]$ ratio is close to unity, whereas the decrease of this ratio is consistent with the β-turn instability. In octreotide (Fig. 3B) the $[\Phi_2]/[\Phi_1]$ ratio varies from ~0.4 to ~0.8 upon increasing concentration, showing that the intermolecular interactions lead to a progressive increase of the turn stability.

The pasireotide CD signal (Fig. 3C) does not share any common feature with those observed in SST-14 and octreotide. A very deep minima around 195 nm is followed at its high wavelength side by two weak bands peaking at ~203 and ~213 nm, and a large positive band at ~230 nm. No concentration dependence in this particular signal was observed in the 50–100 μM range (Fig. 3C). As a consequence, one can definitely rule out the previous assumption, upon which pasireotide and octreotide might possess similar structural features (Interlandi, 2009). Moreover, the pasireotide CD spectrum does not resemble any other characteristic β-turn, such as those previously assigned to the type-I, -I′, -II, -II′, and -VIII (Fuchs et al., 2006; Gibbs et al., 2002; Hernández, Coïc, Gouyette, & Ghomi, 2012; Hernández, Coïc, et al., 2014; Kelly & Price, 2000; Mahalakshimi, Shanmugam, Polavarapu, & Balaram, 2005; Perczel & Fasman, 1992).

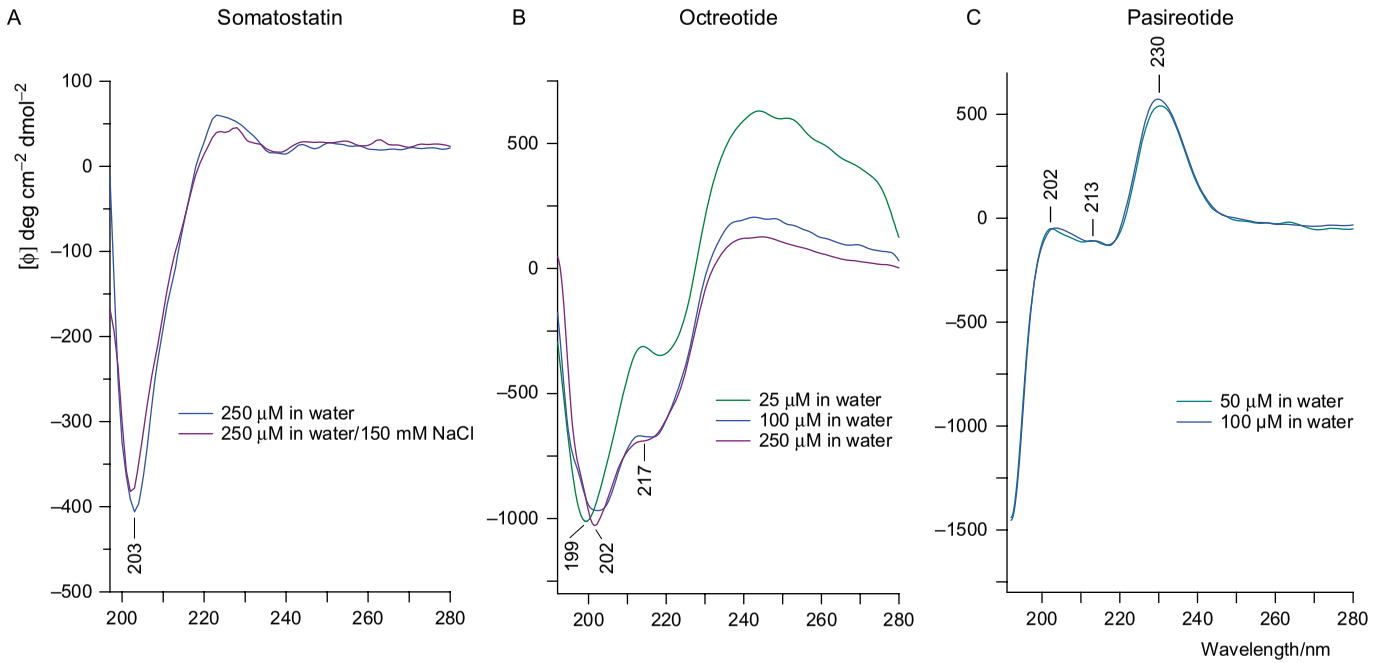

Fig. 3 Circular dichroism spectra of somatostatin-14 (A), octreotide (B), and pasireotide (C) analyzed as a function of concentration in the submillimolar range.

Briefly, while a type-I β-turn provides a CD signal with double minima at ~208/222 nm, resembling that observed in an α-helix, a type-II β-turn is characterized by a positive band located in the 190–210 nm region (Perczel & Fasman, 1992). As far as the reverse β-turn types (i.e., of type-I′ and -II′) are concerned, the CD and NMR spectra recorded in the octapeptides, Boc-Leu-Val-Val-D-Pro-Xxx-Leu-Val-Val-OMe, were consistent with a β-turn formed at their central D-Pro-Xxx. Interestingly, the presence of D-Ala or L-Ala at the position Xxx favors either a stable type-I′ or a type-II′ β-turn, respectively. CD signatures of these peptides observed in methanol and TFE could permit assignment of a large negative band around ~215 nm to the type-I′ β-turn, whereas the type-II′ β-turn was characterized by two partially resolved negative bands with the same intensities, around ~204 and ~218 nm. Finally, the type-VIII β-turn was associated to a CD fingerprint similar to that of type-II′. One can also presume that the particular structure of pasireotide is initiated by the presence of a proline ring included in its Hyp(amec)^{1} residue. This hypothesis can be no more retained, because the cyclic hexapeptide cyclo-(Phe-D-Pro-Gly-Arg-Gly-Asp), giving a CD fingerprint similar to that of octreotide, presents a structural interconversion between the type-II′ and -I′ β-turn (Bour et al., 2008).

The impossibility of assigning a β-turn structural model to pasireotide led us to think about the presence of a more compact fold in this peptide, i.e., a γ-turn. It should be remarked that there exist two γ-turn types, referred to as classical and reverse, one being the mirror image of the other. Both of them correspond to a tight fold appearing on three residues (named i, $i+1$, and $i+2$), and presenting special values for the backbone torsion angles ϕ_{i+1} and ψ_{i+1} (Milner-White, Ross, Ismail, Belhadj-Mostefa, & Poet, 1988). Previously, the combined use of CD, FT-IR absorption, NMR, and classical MD calculations had revealed the formation of a γ-turn in the tripeptide Ala-Phe-Ala (Motta, Reches, Pappalardo, Andretti, & Gazit, 2005). On the basis of a series of experimental and theoretical structural data derived from different tripeptides (unpublished data), we could finally suggest a reasonable model for pasireotide composed by two face-to-face folds: a reverse γ-turn located on the three residues—Phg^{2}-D-Trp^{3}-Lys^{4}—and a type-I β-turn on the four residues—Tyr(Bzl)^{5}-Phe^{6}-Hyp(amec)^{1}-Phg^{2} (Hernández et al., 2016). Fig. 4C displays the suggested structural model for pasireotide, as compared with those suggested for SST-14 (Fig. 4A) and octreotide (Fig. 4B).

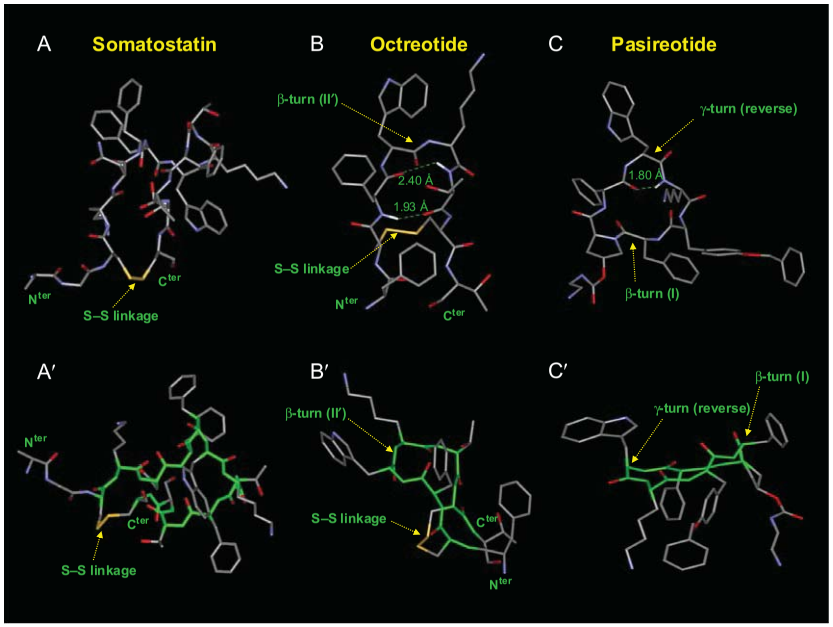

Fig. 4 Graphical representation of the structural models of somatostatin-14 (A and A′), octreotide (B and B′), and pasireotide (C and C′). Two views are selected for each peptide. Hydrogen atoms are removed, except for the molecular groups contributing to intramolecular H-bonds. In A′, B′, and C′ views, the closed part of each peptide is in *green*. Hydrogen bonds are displayed as broken *green lines*, of which the length (in Å) is also reported. Turns and their types, as well as disulfide linkages, are also indicated. *Sources: SST-14: NMR study of SST-14 in 5% D-mannitol. https://www.rcsb.org/pdb/explore.do?structureId=2mi1. The displayed molecule is one of the 10 registered ones, PDB ID: 2MI1. Octreotide: NMR study of the backbone conformational equilibria of sandostatin, minimized average β-sheet structure, PDB ID: 1SOC, http://www.rcsb.org/pdb/explore.do?structureId=1soc. See Hernández, B., López-Tobar, E., Sanchez-Cortes, S., Coïc, Y. M., Baron, B., Chenal, A., et al. (2016). From bulk to plasmonic nanoparticle surfaces: The behaviour of two potent therapeutic peptides, octreotide and pasireotide,* Physical Chemistry Chemical Physics*,* 18*, 24437–24450 for conformational angles and Cartesian coordinates. Pasireotide: DFT-based theoretical calculations. See Hernández, B., López-Tobar, E., Sanchez-Cortes, S., Coïc, Y. M., Baron, B., Chenal, A., et al. (2016). From bulk to plasmonic nanoparticle surfaces: The behaviour of two potent therapeutic peptides, octreotide and pasireotide,* Physical Chemistry Chemical Physics*,* 18*, 24437–24450 for conformational angles and Cartesian coordinates.*

2.1.3 Raman Scattering Structural Fingerprints

In the two last sections, we have emphasized the structural dynamics of the three peptides in the submillimolar concentration range by means of fluorescence and CD data. Here, we follow the structural analysis within the millimolar interval using Raman data. Generally recorded in the middle wavenumber spectral region (1800–400 cm^{-1}), Raman spectra present the advantage of providing a low water contribution (Fig. 5). The solvent background can thus be accurately removed from the peptide Raman spectrum (Fig. 6), enabling an accurate analysis of the molecular vibrational modes.

Owing to their strong modulation of electronic polarizability, the aromatic rings provide strong Raman bands. All three peptides contain a Trp residue, and one (octreotide and pasireotide) or three (SST-14) Phe residues. It should be added that L- and D-stereoisomers provide the same vibrational markers. A previous investigation on the Raman spectra of free amino acids and short peptides has allowed classification and assignment of the most characteristic Trp and Phe markers (Hernández et al., 2010; Hernández, Pflüger, Kruglik, & Ghomi, 2013). One can notice six Phe characteristic bands, referred to as F1, …, F6, and eight Trp bands, named W1, …, W8 (Table 3). Being all localized in Trp and Phe aromatic rings, the

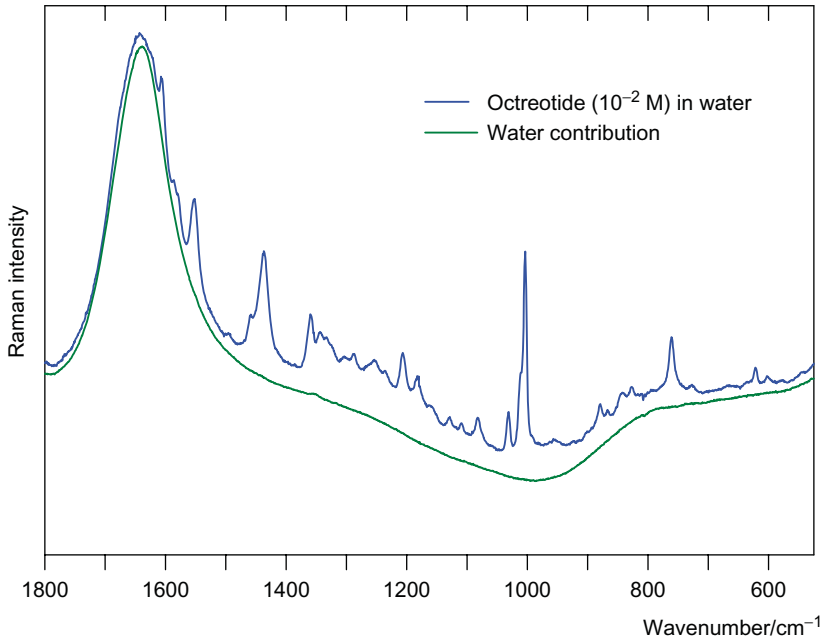

Fig. 5 Raman spectra obtained from the solution sample of octreotide (10^{-2} M) and from the solvent (water).

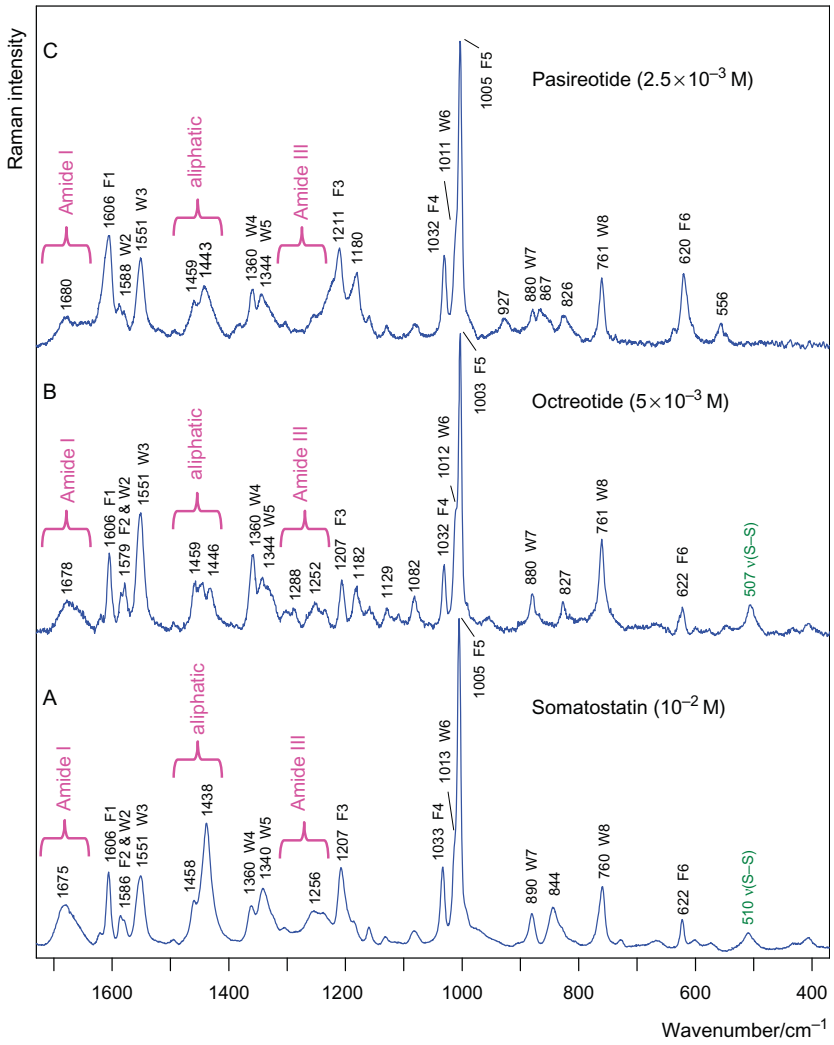

Fig. 6 Comparison of the Raman spectra obtained from the solution samples of somatostatin-14 (A), octreotide (B), and pasireotide (C). Sample concentrations are reported in parentheses. F1–F6 and W1–W8 refer to the characteristic Raman lines of Phe and Trp, respectively. See also Table 3. Amide I and amide III regions, as well as the disulfide marker are also indicated. Sample concentration is reported in parentheses.

wavenumbers of the Trp and Phe markers observed in peptides remain very close to those collected from free amino acids (Table 3). In all cases, the strongest Raman band is F5 (Phe residue) at $\sim$1004 cm^{-1} (Fig. 6), whereas W6 (Trp residue) at $\sim$1012 cm^{-1} is observed as a shoulder at the high wavenumber side of the F5 marker. Despite their aromatic character, the

Table 3 Characteristic Vibrational Modes of Tryptophan and Phenylalanine Observed in Free Amino Acids, Somatostatin-14, Octreotide, and Pasireotide[a]

Free Amino Acid[b]	SST-14@Bulk[c]	SST-14@Ag[d]	Octreotide@Bulk[c]	Octreotide@Ag[d]	Pasireotide@Bulk[c]	Pasireotide@Ag[d]
1621 (W1)						
1606 (F1)	1606 (F1)	1604 (F1)	1606 (F1)	1606 (F1)	1606 (F1)	1608 (F1)
1586 (F2)	1586 (F2 and W2)	1581 (F2 and W2)		1581 (F2 and W2)	1588 (W2)	1580 (F2 and W2, sh)
1579 (W2)			1579 (F2 and W2)			
1552 (W3)	1551 (W3)	1551 (W3)	1551 (W3)	1556 (W3)	1551 (W3)	1553 (W3)
1361 (W4)	1360 (W4)	1362 (W4)	1360 (W4)	1360 (W4)	1360 (W4)	1358 (W4)
1343 (W5)	1340 (W5)	1340 (W5)	1344 (W5)	1344 (W5)	1344 (W5)	1344 (W5)
1207 (F3)	1207 (F3)	1206 (F3)	1207 (F3)	1207 (F3)	1211 (F3)	1210 (F3)
1032 (F4)	1033 (F4)	1031 (F4)	1032 (F4)	1032 (F4)	1032 (F4)	1031 (F4)
1012 (W6)	1013 (W6, sh)		1012 (W6, sh)		1012 (W6, sh)	
1004 (F5)	1005 (F5)	1003 (F5)	1003 (F5)	1005 (F5)	1005 (F5)	1004 (F5)
880 (W7)	890 (W7)	878 (W7)	880 (W7)	880 (W7)	880 (W7)	879 (W7)
758 (W8)	760 (W8)	758 (W8)	761 (W8)	761 (W8)	761 (W8)	761 (W8)
622 (F6)	622 (F6)	622 (F6)	622 (F6)	623 (F6)	622 (F6)	623 (F6)

[a]Observed wavenumbers are in cm^{-1}. In parentheses assignments to tryptophan (W) and phenylalanine (F). *sh*, shoulder.
[b]Vibrational modes of the solution samples containing free amino acids are taken from Hernández, Pflüger, Adenier, Kruglik, and Ghomi (2010).
[c]See Fig. 6 for the bulk Raman spectra of somatostatin, octreotide, and pasireotide.
[d]See Fig. 11 for the SERS spectra of somatostatin, octreotide, and pasireotide adsorbed on silver nanoparticles.

Phg^2 and $Tyr(Bzl)^5$ residues involved in pasireotide do not give rise to resolved and strong Raman markers (Fig. 6C). This might be due to the structural similarity of Phg, as well as the benzyl moiety of $Tyr(Bzl)^5$ with Phe, leading presumably to an overlap of their characteristic markers. In a similar manner, the barely resolved medium intensity bands observed in the 860–840 cm^{-1} region of pasireotide could be assigned to the phenol ring involved in $Tyr(Bzl)^5$ residue (Fig. 6C) (Hernández, Coïc, Pflüger, Kruglik, & Ghomi, 2015).

Raman spectra can provide valuable structural information through their amide I (1700–1640 cm^{-1}) and amide III (1305–1230 cm^{-1}) regions. It should be emphasized that amide I vibrations result from the backbone C═O bond-stretch motion, more or less coupled to its adjacent N—H angular bending. Amide III vibrations basically arise from the backbone N—H angular bending. As a consequence, upon labile hydrogen deuteration (Raman spectra observed in heavy water), amide I vibrations present a $\sim$10 cm^{-1} downshift, whereas amide III markers completely vanish. Both amide (I and III) regions are shown to be conformation sensitive, i.e., specific amide markers can be assigned to α-helix, β-strand/β-sheet, turns, and unordered segments of a peptide chain. Based on a series of analyses made on peptides and proteins, we could propose rational band decomposition in order to achieve the estimation on the populations corresponding to different secondary structural elements (Boukhalfa-Heniche et al., 2004; Guiffo-Soh, Hernández, Coïc, Boukhalfa-Heniche, & Ghomi, 2007; Guiffo-Soh et al., 2008; Hernández, Boukhalfa-Heniche, Seksek, Coïc, & Ghomi, 2006; Hernández et al., 2009; Hernández, Coïc, et al., 2014; Hernández, Coïc, Gouyette, et al., 2012; Hernández, Coïc, Kruglik, et al., 2012; Hernández et al., 2016). Here, four amide I components and five amide III components have been used (Table 4; Fig. 7).

Table 4 Components Used in the Decomposition of Amide I and Amide III Regions, and Their Assignments[a]

Amide I	Amide III	
1690 ± 5	1260 ± 5	Random chain (R)
1660 ± 5	1235 ± 5	β-Strand (S)
1675 ± 5	1305 ± 5	Turn (T)
1650 ± 5	1285 ± 5	Turn (T)
	1250 ± 5	Turn (T)

[a]The band width of each component was kept between 15 and 25 cm^{-1}.

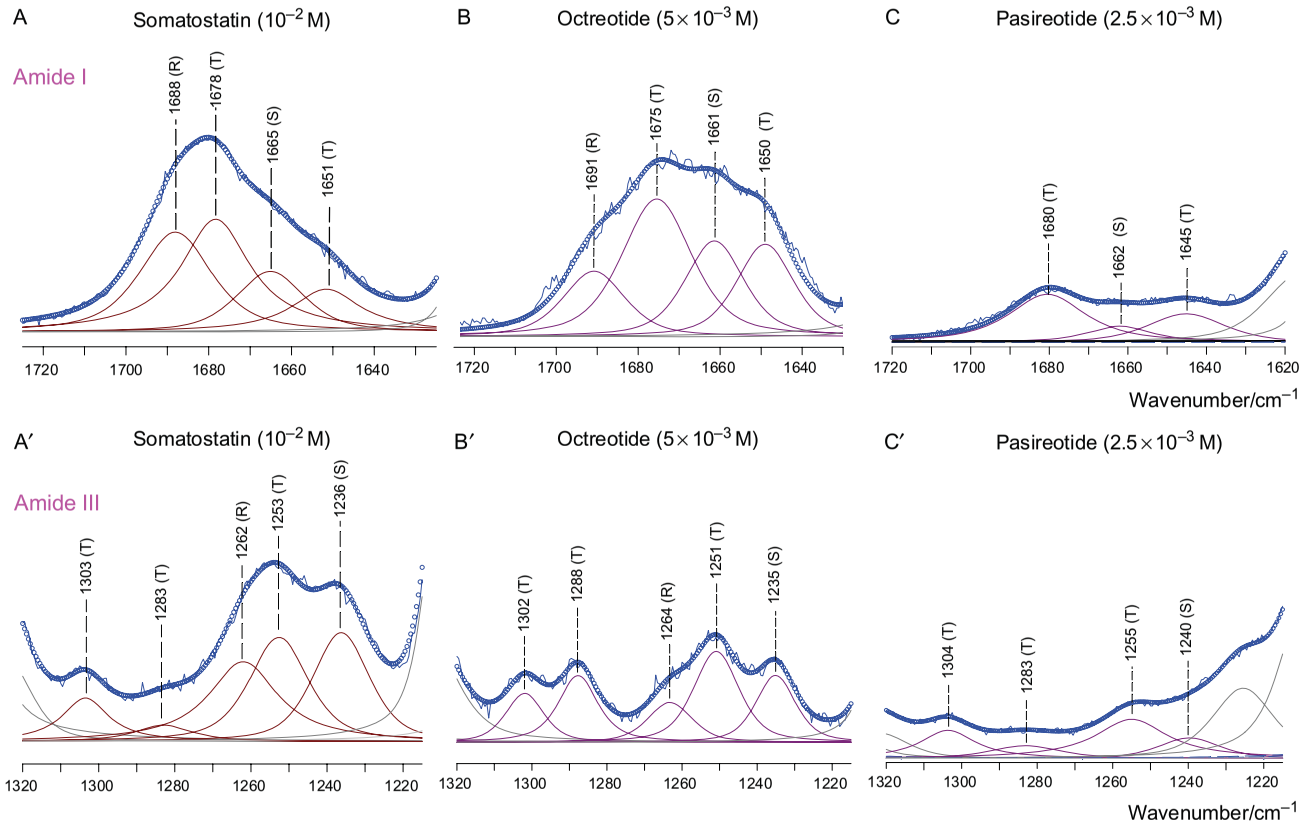

Fig. 7 Band decomposition of the amide I (A, B, and C) and amide III (A′, B′, and C′) of the Raman spectra obtained from the solution samples of SST-14 (A and A′), octreotide (B and B′), and pasireotide (C and C′). In front of each component wavenumber, its assignment to random (R), β-strand (S), and turn (T) is reported. *Circles* correspond to the sum of the components used in the band decomposition.

The histogram presented in Fig. 8 clearly shows that upon increasing concentration the weight (population) of unordered chain decreases in favor of the progressive increase of the β-strand population. In contrast, the turn population manifests a quite constant stability. This effect is more pronounced in SST-14, because of the large size of its turn. It is worth mentioning that pasireotide revealed no detectable unordered population, because of the absence of the amide I component at $\sim 1690\,cm^{-1}$, and the amide III component at $\sim 1265\,cm^{-1}$ in band decomposition. In pasireotide, the turn population is as high as ~84%; the remaining ~16% population corresponds to β-strand, confirming the rigid structural model proposed for this compound (Fig. 4C and C′).

The concentration-induced structural dynamics of disulfide-containing peptides, such as SST-14 and octreotide, can also be followed through the Raman markers appearing in the $550–500\,cm^{-1}$ spectral region (Fig. 9),

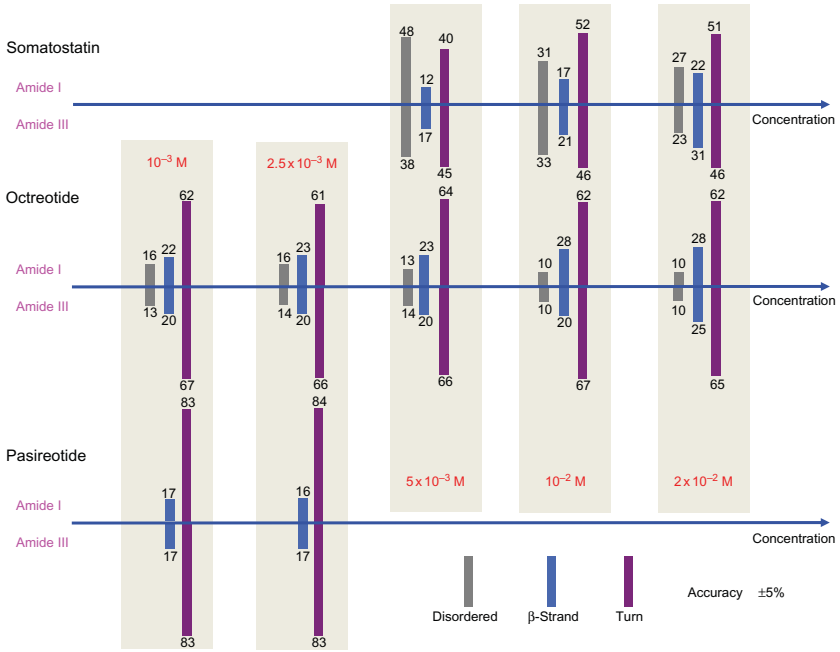

Fig. 8 Histogram representing the normalized weight (population) of different secondary structural elements (disordered, β-strand and turn) obtained by band decomposition in the amide I and amide III regions. From *top* to *bottom*, on each axis are displayed the results corresponding to one of the three analyzed peptides. Data corresponding to the amide I region are indicated above, and those related to the amide III region are reported beneath the same axis. Increasing concentration from *left* to *right*.

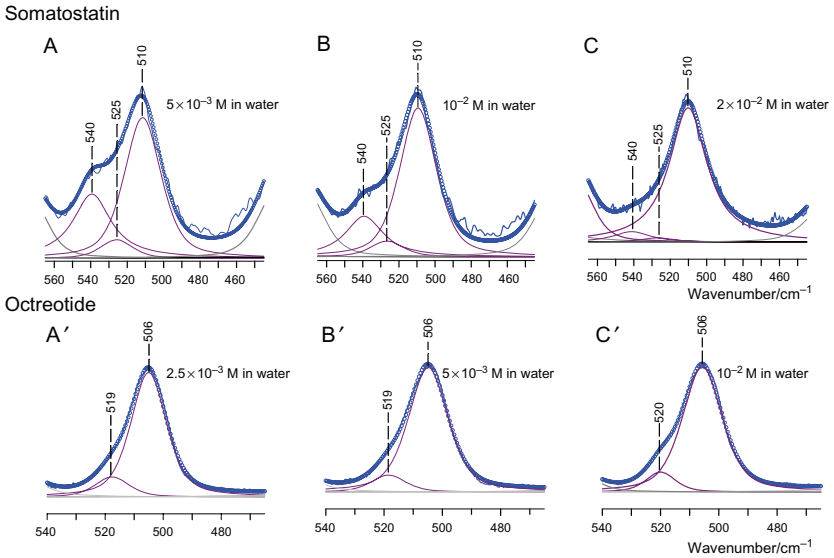

Fig. 9 Band decomposition of the disulfide bond-stretch region observed in the bulk Raman spectra of SST-14 (A, B, and C) and octreotide (A′, B′, and C′). *Circles* correspond to the sum of the components used in decomposition. Increasing concentration is from *left* to *right*. Sample concentration is reported.

which reveals the S—S bond-stretch motion within the Cys-Cys (cystine) moiety formed by the oxidative reaction of the Cys thiol groups. The conformational sensitivity of the S—S bond vibrational motions was evidenced since the earliest Raman studies on simple molecular models (Sugeta, Go, & Miyazawa, 1972; Van Wart & Scheraga, 1976, 1986). Based on these studies, it had been postulated that the Raman marker assigned to the S—S bond-stretch vibration is dependent on the values of the three torsion angles defined around the three successive bonds along the cystine —C—S—S—C— motif. As a consequence, the three frequently observed bands at ~510, ~525, and ~540 cm^{-1} were assigned to *ggg*, *ggt*, and *tgt* orientations (where *g*, *gauche* and *t*, *trans*) of the three mentioned torsion angles. It is worth emphasizing that the structural rigidity, brought about by the concentration increase, can affect the conformational flexibility of the turn and its closing disulfide bridge. While the Raman spectrum of SST-14 at the lowest concentration (5 mM) reveals three components at 510, 525, and 540 cm^{-1} (Fig. 9A), those obtained at higher concentrations (10 and 20 mM) show a considerable decrease of the components at 525 and 540 cm^{-1} (Fig. 9B and C). In other words, the concentration increase permits stabilization of the disulfide bridge in a conformation assignable to the 510 cm^{-1} marker. In octreotide,

no remarkable change could be observed in the disulfide region. As shown in Fig. 9A′–C′, the components at 506 and 519 cm^{-1} remain unchanged in the concentration range between 2.5 and 20 mM, revealing the structural stability of its type-II′ β-turn. Note that in octreotide, no component close to 540 cm^{-1} could be found in the mentioned concentration range.

A recent analysis devoted to the disulfide linkage Raman markers has shown that the above-mentioned traditional interpretation based on "three Raman markers vs three conformations" appears to be insufficient for achieving a reliable relationship between the multicomponent Raman bands and the disulfide bridge conformational flexibility (Hernández et al., 2014). A new assumption has been suggested, inspired from a former statistical analysis of the protein data bank (Hogg, 2013; Schmidt, Ho, & Hogg, 2006; Schmidt & Hogg, 2007). This analysis has pointed out the fact that an accurate treatment of a disulfide bridge conformation needs the full consideration of the signs associated to the five torsion angles, referred to as χ_1, χ_2, χ_3, χ_2', χ_1', defined around the five successive bonds in the —Cα—Cβ—S—S—Cβ′—Cα′— segment of cystine. For instance, the ± sign attributed to χ_3 (defined around the S—S bond) determines the handedness (right or left) of the disulfide bridge; the signs of the three middle angles χ_2, χ_3, and χ_2' are related to the disulfide spatial shape, referred to as Staple-, Hook-, and Spiral-like disulfides; and finally the ± signs assigned to the two extreme angles, i.e., χ_1 and χ_1', are responsible for the orientation of the disulfide linkage with respect to peptide backbone(s). Based on this methodology, density functional theory calculations revealed that the S—S bond-stretch wavenumber may cover a large spectral range from 469 to 553 cm^{-1} (Hernández, Pflüger, et al., 2014). Specifically, in SST-14 and octreotide, one can assign the components at ∼506 and 510 cm^{-1} (Fig. 9) to ±LHStaple and −LHHook conformers, respectively; the component at ∼525 cm^{-1} to +RHHook-type conformer; and finally the component at ∼540 cm^{-1} to ±LHSpiral conformer. In these notations, the left side ±, −, and + signs refer to χ_1 and χ_1', while RH and LH designate right- and left-handed disulfide bonds, respectively.

2.2 Adsorption of SST-14 and Its Analogues Onto Silver Nanoparticles

Because of the silver chemical reactivity, the major drawback encountered in the adsorption of SST-14 and octreotide on silver nanoparticles (AgNPs) was the breakdown of their disulfide bond. Thus, a special attention was focused on the preparation protocol of silver colloids, especially on the

choice of reductant. In a series of investigations, the integrity of the disulfide linkage on AgNPs was checked by means of SERS data (Hernández et al., 2016; López-Tobar et al., 2015; López-Tobar, Hernández, Ghomi, & Sanchez-Cortes, 2013).

2.2.1 Aggregation of AgNPs Provoked by the Adsorption of SST-14 and Its Analogues

Silver colloids present a sharp plasmon resonance band peaking at ~400 nm (Fig. 10A). To induce aggregation of AgNPs, an ionic salt (KNO_3, NaCl, etc.) is generally added to the colloidal solution sample. In fact, this operation leads to screening negative charges at the surface of colloids by the positively

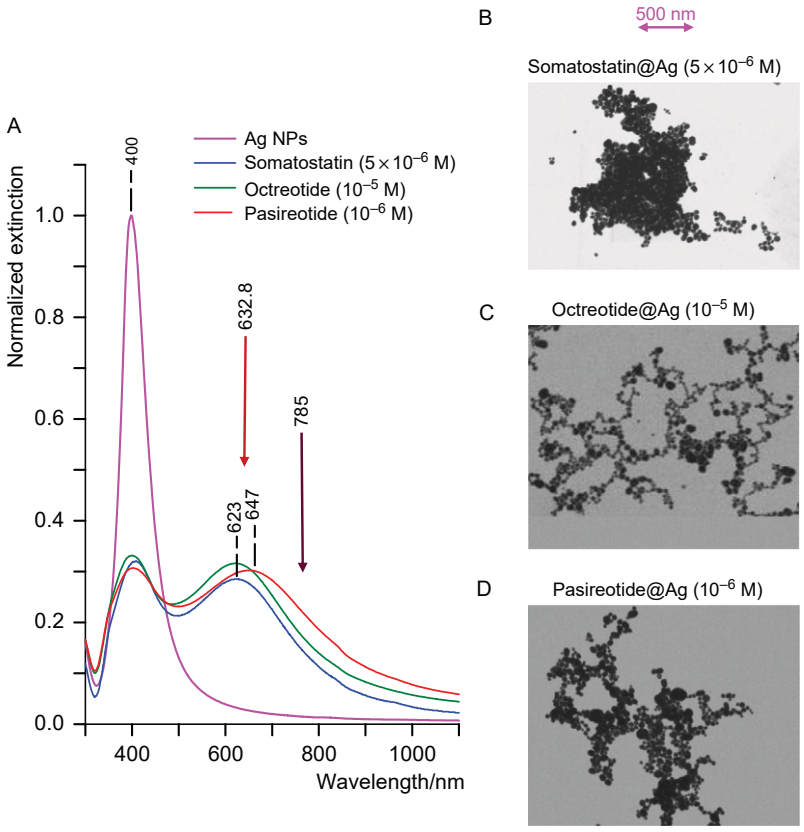

Fig. 10 Normalized extinction spectra of silver colloids alone, and in the presence of SST-14, octreotide, and pasireotide (A). TEM images taken from the same samples containing AgNPs in the presence of SST-14 (B), octreotide (C), and pasireotide (D) are also reported. Sample concentration is reported in *parentheses*.

charged counterions. As a consequence, the repulsive electrostatic interaction between NPs is reduced, facilitating their aggregation. In the case of SST-14 and its analogues, no aggregating agent was needed, because they are all of cationic character. SST-14 can bear up to three positive charges (N^{ter}, Lys^4, and Lys^9). Likewise, octreotide (N^{ter} and Lys^5) and pasireotide (Lys^4 and $Hyp(amec)^1$) may contain two positive charges.

Upon interaction with peptides, the plasmon resonance of AgNPs shows a large redshift (~230 nm), making appear a new large band between 620 and 640 nm (Fig. 10A). As shown, the optimal plasmon band shift is obtained by a low peptide concentration corresponding to the 10^{-5}–10^{-6} M range (Fig. 10A). Transmission electron microscopy (TEM) images confirm the aggregation of Ag colloids interacting with the three cationic peptides (Fig. 10B–D).

2.2.2 SERS Induced by SST-14 and Its Analogues Adsorbed on AgNPs

The amplification of the Raman signal in SERS experiments is greatly due to the formation of the so-called hot spots, i.e., narrow interparticle junctions formed upon AgNP aggregation (Fig. 10B–D). Within the hot spots, both incident and scattered radiations are considerably amplified (Chen, Ding, Luo, Loo, & Yao, 2015; Guerrini, Izquierdo-Lorenzo, Garcia-Ramos, Domingo, & Sanchez-Cortes, 2009), provided that the incident wavelength falls into the plasmon band of aggregated NPs. Fig. 10A shows the position of the two excitation wavelengths, i.e., $\lambda_L = 632.8$ and 785 nm, being in resonance with the large plasmon band appearing upon interaction with peptides.

Fig. 11 displays the SERS spectra of SST-14 at 5×10^{-6} M, octreotide at 10^{-5} M, and pasireotide at 10^{-6} M, adsorbed on Ag particles. The very good signal/noise ratio of SERS spectra allows us to follow the changes occurring in Raman spectra in going from bulk (Fig. 6) to AgNP surface (Fig. 11). A striking similarity is found between the SERS and bulk Raman spectra. For instance, the wavenumbers, as well as the relative intensities of the characteristic Trp and Phe characteristic bands, remain very close to those observed in bulk (Fig. 6; Table 3). It should be emphasized that in SERS spectra, the amide I and amide III regions cannot be compared to those observed in bulk, because only the signal from the backbone segments that are close to metal surface is enhanced. As a consequence, these spectral regions cannot provide reliable information on the whole backbone structural features. The presence of the low-intensity bands located at 498 cm^{-1} in SST-14 (Fig. 11C) and at 506 cm^{-1} in octreotide (Fig. 11B) proves the integrity of the disulfide linkage upon adsorption.

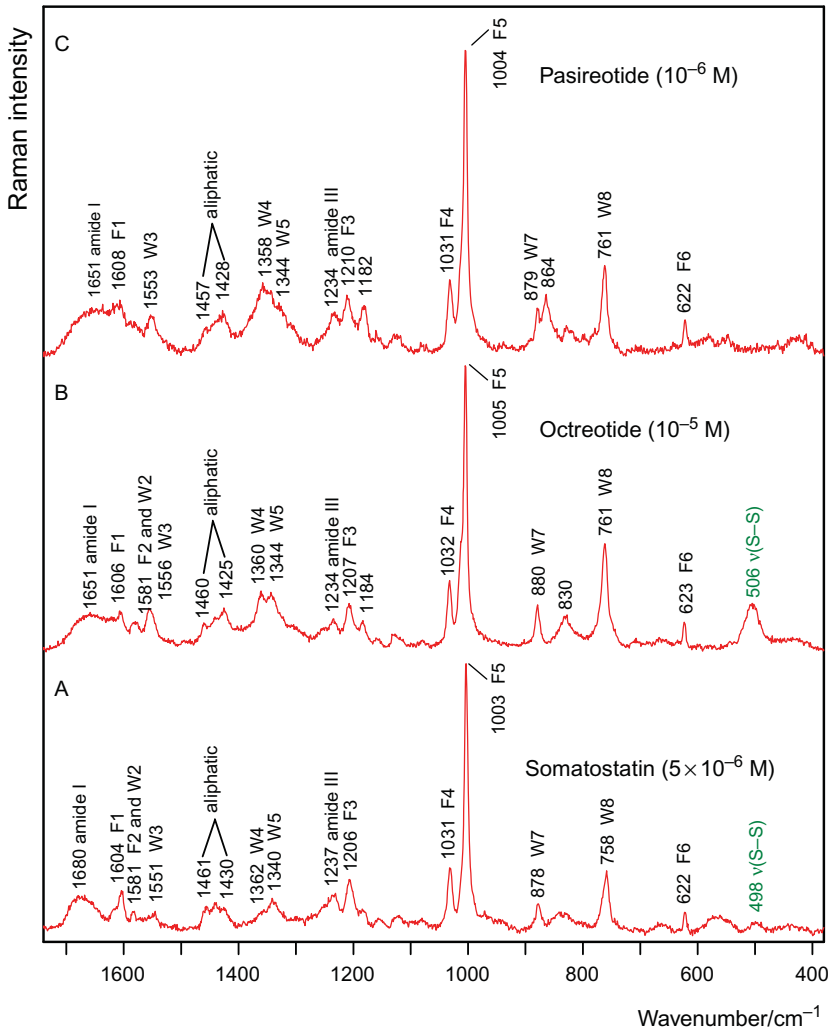

Fig. 11 Comparison of the surface-enhanced Raman spectra obtained from the solution samples of somatostatin-14 (A), octreotide (B), and pasireotide (C). F1–F6 and W1–W8 refer to the characteristic Raman lines of Phe and Trp, respectively. See also Table 3. Amide I and amide III regions as well as the disulfide marker are indicated. Sample concentration is reported in parentheses.

2.2.3 Anchoring Sites of SST-14 and Its Analogues on AgNPs

On the basis of the information provided by the SERS data in the middle wavenumber region (Fig. 11), we can confirm that the aromatic (Phe and Trp) residues cannot be considered as the potential binding site of

SST-14 and its cyclic analogues to AgNPs. The low wavenumber spectral region ($<300\,cm^{-1}$) is known for its capability of providing complementary information on the binding mechanism through the vibrational motions involving metal atoms (Cañamares, Garcia-Ramos, Gómez-Varga, Domingo, & Sanchez-Cortes, 2005; Garrell, Shaw, & Krimm, 1983). Thanks to the presence of Cl^- ions at the surface of silver colloids, a middle intensity SERS marker is observed at $\sim 245\,cm^{-1}$, ascribed to Ag-Cl^- bond-stretch motion. Fig. 12A clearly shows the presence of a unique band in the case of AgNPs aggregated by addition of KNO_3. This band also appears when the silver particles are aggregated by means of peptides (Fig. 12B–D). Strikingly, in the presence of peptides, a new component appears at ~ 220 nm. This observation leads us to deduce that there should be two types of Ag-Cl^- vibrations, one of them unperturbed and the other perturbed by the interaction with peptides adsorbed on AgNPs. Surely, this perturbation should be of electrostatic character, presumably between Cl^- anion and one of the cationic sites (NH_3^+) of the adsorbed peptide.

Based on the provided evidences, three possible adsorption schemes can be suggested for SST-14, i.e., through its Lys^4 (Fig. 13A), Lys^9 (Fig. 13B), or N^{ter} group (Fig. 13C). Likewise, in octreotide the adsorption can be made possible by the intermediate of either Lys^5 (Fig. 14A) or N^{ter} group (Fig. 14B). Finally, in pasireotide, Lys^4 (Fig. 14C) and $Hyp(amec)^1$ (Fig. 14D) can contribute to stabilize the peptide/NP interactions.

3. CONCLUDING REMARKS

3.1 Bulk Structural Dynamics

Because of their particular chemical structure, peptide chains are able to self-assemble upon increasing concentration. Interpeptide interactions are generally stabilized by the formation of interbackbone —C═O...H—N— hydrogen bonds, giving rise to parallel or antiparallel β-sheet structures. Peptide self-assemblies can be further stabilized by other interaction types, such as aliphatic–aliphatic, aliphatic–aromatic, aromatic–aromatic, polar, and electrostatic interactions. In this framework, the structuring role of surrounding water molecules should also be taken into consideration (Otting, Liepinsh, & Wüthrich, 1991; Zhong, Pal, & Zewail, 2011).

As far as SST-14 and its analogues are considered, at low concentrations, i.e., in the submillimolar range, fluorescence anisotropy measurements were consistent with a high rotational freedom of their

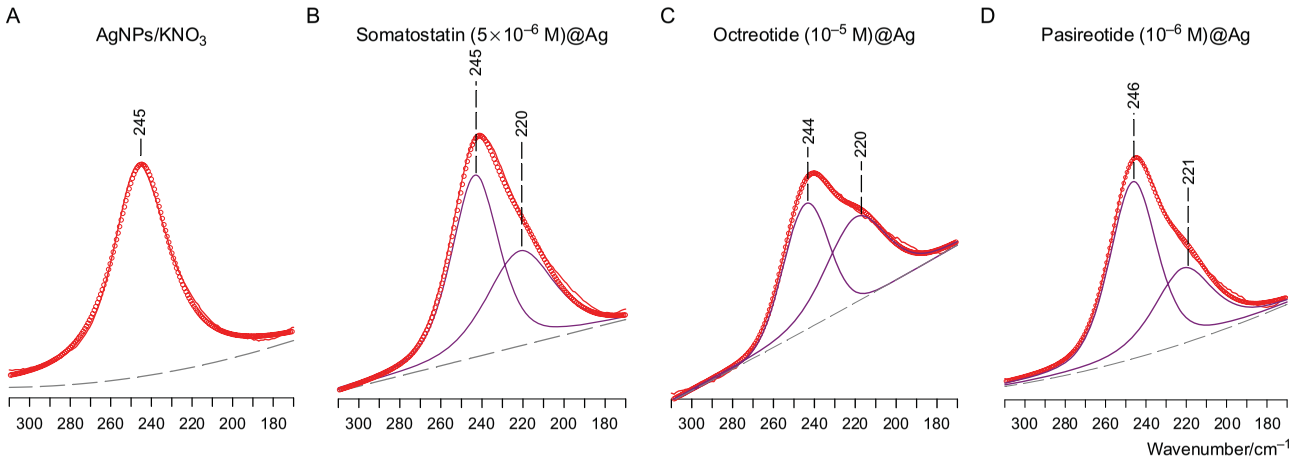

Fig. 12 Band decomposition of the low wavenumber ($<300\,cm^{-1}$) region observed in the surface-enhanced Raman spectra of AgNPs aggregated upon addition of KNO_3 (A), SST-14 (B), octreotide (C), and pasireotide (D). *Circles* correspond to the sum of the components used in decomposition. Sample concentration is reported in *parentheses*.

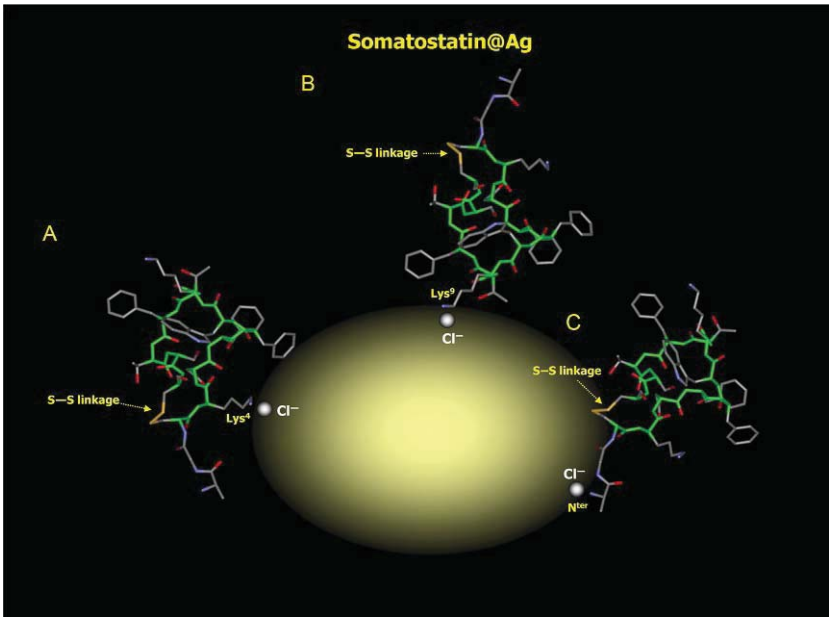

Fig. 13 Binding schemes of SST-14 on silver nanoparticles. The peptide hormone is stabilized on AgNPs by means of the electrostatic interactions involving the negatively charged chloride ions on the plasmonic surface and the positively charged amino group borne by Lys^4 residue (A), Lys^9 residue (B), or N^{ter} group (C).

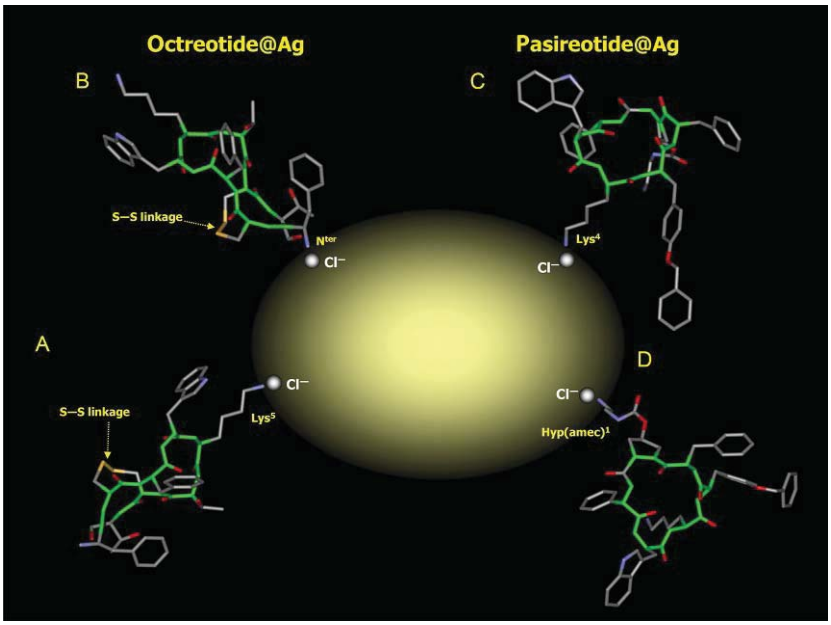

Fig. 14 Binding schemes of octreotide (A and B) and pasireotide (C and D) on silver nanoparticles. Octreotide is stabilized on AgNPs by means of the electrostatic interactions involving the negatively charged chloride ions on the plasmonic surface and the positively charged amino group borne by either Lys^5 residue (A) or N^{ter} group (B). Pasireotide is stabilized on AgNPs through the positively charged amino group borne by either Lys^5 residue (C) or $Hyp(amec)^1$ residue (B).

unique Trp residue. This feature might certainly facilitate the binding of these peptides to SSTRs, in which Trp-Lys adjacent residues should play a key role (Weckbecker et al., 2003). In this range of concentration, SST-14 remains unordered, whereas octreotide and pasireotide adopt stable cyclic structures. As a consequence, the longer and more flexible chain of SST-14 confers this peptide hormone the propensity of binding quite equivalently to its five receptors. In contrast, octreotide, having a shorter turn and more rigid structure, was shown to have a pronounced affinity for SSTR2, and a moderate one for both SSTR3 and SSTR5 (Pawlikowski & Meleń-Mucha, 2004; Weckbecker et al., 2003). Concerning pasireotide, it targets strikingly four out of five SSTRs, with the highest affinity for SSTR5 (Bruns, Lewis, Briner, Meno-Tetang, & Weckbecker, 2002).

Upon increasing the concentration up to the millimolar range, SST-14 becomes progressively structured, i.e., the rate of unordered chain decreases in favor of H-bonded β-strands. At 20 mM, only ~20% of total structural elements correspond to unordered chains. The unordered-to-ordered structural trend is less pronounced in octreotide. Above 10 mM, the unordered chain population of this peptide remains around 10%. In contrast, no indication on unordered structure could be evidenced in pasireotide. A highly rigid cyclic structure was evidenced in the whole micromolar–millimolar concentration interval.

In relation with the fact that peptide/protein hormones are stored as amyloids within secretory granules, dynamical behavior of SST-14 at higher concentrations has also received a considerable attention (Maji et al., 2009; van Grondelle et al., 2007). Recent studies highlighted the spontaneous formation of nanofibrils by gradual SST-14 aggregation in the 15–60 mM concentration range. Nanofibrils are thought to be stabilized by the interaction of side-by-side molecules, forming interpeptide antiparallel H-bonded strands. Above 60 mM, nanofibrils give progressively rise to extended nanofibers upon formation of parallel interchain H-bonds (van Grondelle et al., 2013). Although the disulfide linkage was shown to have no evident effect on the structural dynamics of the peptide hormone at low (submillimolar) concentrations (Hernández et al., 2009), its presence was revealed essential on the nature and morphology of amyloids, as well as on their aggregation/release kinetics (Anoop et al., 2014). No high concentration-induced aggregation analysis has been reported up to now on octreotide. Evidently, such type of exploration cannot be envisaged in pasireotide because of its low water solubility above 2.5 mM.

3.2 Toward Somatostatin-Based Functionalization of Plasmonic NPs

We have shown that the three cationic peptides (SST-14 and its two cyclic analogues) manifest a high affinity for binding spontaneously to the surface of hydroxylamine-reduced AgNPs. This binding does not cause the breakdown of the disulfide bridge in SST-14 and octreotide. The peptide/NP binding process is rendered possible by electrostatic interactions, occurring between the positively charged amino groups of the peptide and the chloride anions covering the colloidal surface. Beyond a considerable plasmon resonance shift, an important amplification of the SERS intensity, ranging between 10^4 and 10^5, was provoked by peptide adsorption, allowing detection of trace amounts (10^{-5}–10^{-6} M) of the peptides in aqueous solution.

During the recent years, it has been noticed that a better addressability of cellular targets and tumor cells can be achieved by the use of functionalized NPs. Limiting our scope to plasmonic NPs, and especially to their functionalization either with somatostatin, or with its analogues, we can mention here some in vitro experiments: (i) The cellular uptake by means of somatostatin-coated AuNPs on HCC-1806, HELA, and U-87 cell lines has been revealed to be significantly higher than that achieved by non-functionalized particles (Abdellatif et al., 2016). (ii) The temperature increase induced by irradiation at 532 nm (i.e., into the plasmonic resonance band) of octreotide-coated AuNPs during 5 ns leads to a notable decrease of HELA cells viability (Mendoza-Nava et al., 2013). (iii) Radiolabeled AuNPs may function simultaneously as radiotherapy and thermal ablation systems. A multifunctional protocol was thus tested as follows: Lys^3-bombesin, a peptide having a high affinity for GRP-R receptor (overexpressed in prostate cancer), and a cell penetrating peptide, HIV Tat(49–57) reaching DNA, were conjugated to $^{99m}Tc/^{177}Lu$-labeled AuNPs and tested on PC3 cancer cells. Internalization, followed by irradiation at 532 nm, resulted in a significant decrease of PC3 viability down to 1.3% (Jiménez-Mancilla et al., 2013).

Nevertheless, the application of somatostatin-based functionalized plasmonic NPs for in vivo purposes needs further attention, especially for avoiding the formation of the so-called protein corona around these particles when they are found in biological fluids (Casals, Pfaller, Duschl, Oostingh, & Puntes, 2010; Walkey et al., 2014). To minimize this effect a number of polymer-coated NPs were elaborated (Khan, Gupta, & Nandi, 2013; Pelaz et al., 2015). Recently, the silver-decorated gold nanorods have been successfully used to deliver specific targeted chemotherapy against both MCF7 and PC3 cell lines. In these experiments, doxorubicin, a commonly used

chemotherapy, and an antiepithelial cell adhesion molecule antibodies were covalently bound to thiolated polyethylene glycol (PEG)-coated AuNR\Ag. The resultant system was used to deliver chemotherapy drugs to cancer cells (Nima et al., 2017).

4. MATERIAL AND METHODS

4.1 Peptides

Somatostatin-14 (SST-14, Fig. 1A) was purchased from Sigma-Aldrich (Lyon). Octreotide (Fig. 1B) was synthesized by solid-phase peptide synthesis at the Institut Pasteur (Paris, France), following the Fmoc/*t*Bu methodology. The details of this chemical synthesis were reported previously (Hernández, Coïc, Kruglik, et al., 2012). Pasireotide (Fig. 1C) was a gift from Novartis Pharma (Basel). Purity of the three peptides was checked by RP-HPLC. Respective masses of the peptides were determined by mass spectroscopy as follows: SST-14 monoisotopic $[M+H]^+$ 1637.72 d, observed 1637.76 d (Hernández et al., 2009); octreotide $[M+H]^+$ 1019.45 d, observed 1019.46 d (Hernández, Coïc, Kruglik, et al., 2012); pasireotide monoisotopic $[M+H]^+$ 1047.51 d, observed 1047.73 d (Hernández et al., 2016).

4.2 Sample Preparation

4.2.1 Solution Samples of Peptides

Lyophilized powder of peptides was dissolved in pure water from a Millipore filtration system (Guyancourt). Sodium chloride purchased from Merck (Fontenay-sous-Bois) was added to the solution samples, if necessary. 5 mM stock solutions of SST-14 and octreotide were prepared, i.e., at 8.2 mg/mL (SST-14) and 5.5 mg/mL (octreotide), and further diluted to reach the final concentrations needed for CD, fluorescence, and SERS experiments. In pasireotide, taking into account its water solubility, the maximum concentration giving rise to a limpid solution was 2.5 mM (2.6 mg/mL). This sample was the most concentrated one for recording the bulk Raman spectra; it served as stock solution for other experiments needing lower concentrations.

4.2.2 AgNPs Used as Substrates for Peptide Adsorption

AgNP suspension was elaborated by adding 300 mL of sodium hydroxide (Sigma-Aldrich, Lyon) solution (1 M) to 90 mL of a 6×10^{-2} M hydroxylamine hydrochloride (Sigma-Aldrich, Lyon) solution. Then 10 mL of a 1.11×10^{-3} silver nitrate (Sigma-Aldrich, Lyon) aqueous solution was added dropwise to the mixture under vigorous stirring. The solution

containing silver colloids turned to brown. Using this protocol, polydisperse colloids are generally obtained, as evidenced by the TEM images in Fig. 10. AgNPs were aged 1 week at 4°C before use. Upon addition the solution containing a cationic peptide to colloidal solution, the color turns to dark gray, revealing AgNPs aggregation. UV–visible and Raman spectra were recorded just after sample preparation.

4.3 Experimental Setups

4.3.1 Fluorescence

Room temperature fluorescence spectra were recorded on a PTI Quanta-Master QM4CW spectrofluorometer (Lawrenceville, NJ) at 25°C using a quartz cell with 10 mm path length. Bandwidths were set to 1 and 5 nm for excitation and emission, respectively. Values corresponding to anisotropy measurements were 5 and 15 nm, respectively. Fluorescence anisotropy, $\langle r \rangle$, was estimated by the relation: $\langle r \rangle = \frac{I_{VV} - GI_{VH}}{I_{VV} + 2GI_{VH}}$, where the G factor is: $G = \frac{I_{HV}}{I_{HH}}$, and I denotes the polarized intensity corresponding to the vertical (V) and horizontal (H) polarization states (with respect to the plane including the incident and fluorescence beams, also referred to as scattering plane) of the excitation (first subscript) and emission (second subscript) radiations (Lackowicz, 2006).

4.3.2 Circular Dichroism

Room temperature CD spectra were analyzed on a JASCO J-810 spectrophotometer (Lisses) within the 190–300 nm spectral region. A path length of 1 mm and a spectral resolution of 0.2 nm were selected. Each spectrum corresponding to an average of five scans was recorded with a speed of 100 nm per min. The measured ellipticity for each sample, referred to as $[\phi]_{obs}$, was further normalized to obtain the so-called mean residue ellipticity, $[\phi]$, by using the expression: $[\Phi] = \frac{[\Phi]_{obs}}{ncl}$, where n, c, and l are the number of residues in the peptide, the molar concentration, and the optical path length of the sample, respectively (Lazo & Downing, 2001). The normalized ellipticity was expressed in deg cm^2 dmol^{-1}.

4.3.3 Ultraviolet–Visible Absorption

UV–visible spectra of silver colloids, alone or in the presence of peptides, were recorded at room temperature on a Shimadzu 3600 UV–visible absorption spectrometer (Duisburg) by means of quartz cells having an optical path of 1 cm.

4.3.4 Transmission Electron Microscopy

TEM images were taken at room temperature using a JEOL JEM-2010 electron microscope (Croissy) with an acceleration voltage of 200 kV. The samples were prepared by depositing 10 μL of the suspension containing either AgNPs or their complexes with the peptides, on carbon-coated Cu grids (ref. G400-Cu).

4.3.5 Bulk Raman Scattering

Room temperature Stokes Raman spectra were analyzed at right angle on a Jobin-Yvon T64000 spectrometer (Longjumeau) at single spectrograph configuration, 1200 grooves/mm holographic grating, and a holographic notch filter. Raman data corresponding to 1200 s acquisition time for each spectrum were collected on a liquid nitrogen cooled CCD detection system (Spectrum One, Jobin-Yvon). The effective slit width was set to 5 cm^{-1}. Solution samples were excited by the 488 nm line of an Ar^{+} laser, Spectra Physics (Evry), with 200 mW power at the sample.

4.3.6 Surface-Enhanced Raman Scattering

SERS data were collected on a Renishaw Raman inVia spectrometer (Champs-sur-Marne) equipped with an electrically cooled CCD camera. Samples were excited by means of the 632.8 or 785 nm line of a diode laser with an output power of 18 mW at the sample, and 1200 grooves per nm holographic grating. The spectral resolution was 2 cm^{-1}, with a total acquisition time of 10 s for each SERS measurement.

4.3.7 Spectroscopic Data Posttreatment

Buffer subtraction and smoothing of the observed spectra were performed using the GRAMS/AI Z.00 package (Thermo Galactic, Waltham, MA). The analysis of some composite bands was performed by curve fitting using pseudo-Voigt (Gaussian + Lorentzian) functions, with the Lorentzian contribution kept equal to or greater than 50%. Final presentation of Raman spectra was done by means of SigmaPlot package 6.10 (SPSS Inc., Chicago, IL).

ACKNOWLEDGMENTS

The authors would like to thank Novartis Pharma (Basel, Switzerland) to have generously provided the lyophilized sample of pasireotide. This work was supported by the Spanish *Ministerio de Economía y Competitividad* (Project FIS 2014-52212-R). Quantum mechanical calculations were granted access to the HPC resources of CINES/IDRIS under the allocation 2017-A0010805065 made by GENCI (*Grand Equipement National de Calcul Intensif*).

REFERENCES

Abdellatif, A. A., Zayed, G., El-Bakry, A., Zaky, A., Saleem, I. Y., & Tawfeek, H. M. (2016). Novel gold nanoparticles coated with somatostatin as a potential delivery system for targeting somatostatin receptors. *Drug Development and Industrial Pharmacy*, *42*, 1782–1791.

Agnihotri, S., Mukherji, S., & Mukherji, S. (2014). Size-controlled silver nanoparticles synthesized over the range 5–100 nm using the same protocol and their antibacterial efficacy. *RSC Advances*, *4*, 3974–3983.

Anoop, A., Ranganathan, S., Dhaked, B. D., Jha, N. N., Pratihar, S., Ghosh, S., et al. (2014). Elucidating the role of disulfide bond on amyloid formation and fibril reversibility of somatostatin-14. Relevance to its storage and secretion. *The Journal of Biological Chemistry*, *289*, 16884–16903.

Aslan, K., Lakowicz, J. R., & Geddes, C. D. (2005). Plasmon light scattering in biology and medicine: New sensing approaches, visions and perspectives. *Current Opinion in Chemical Biology*, *9*, 538–544.

Barrio, M., Czernin, J., Fanti, S., Ambrosini, V., Binse, I., Du, L., et al. (2017). The impact of somatostatin receptor-directed PET/CT on the management of patients with neuroendocrine tumor: A systematic review and meta-analysis. *Journal of Nuclear Medicine*, *58*, 756–761.

Bastús, N. G., Comenge, J., & Puntes, V. (2011). Kinetically controlled seeded growth synthesis of citrate-reduced nanoparticles of up to 200 nm: Size focusing versus Ostwald ripening. *Langmuir*, *27*, 11098–11105.

Beschiaschvilli, G., & Seeling, J. (1991). Peptide binding to lipid membranes. Spectroscopic studies on the insertion of a cyclic somatostatin analog into phospholipid bilayers. *Biochimica et Biophysica Acta*, *1061*, 78–84.

Bhattacharyya, K., & Basak, S. (1995). Somatostatin in a water-restricted environment: Fluorescence and circular dichroism study in AOT reverse micelles. *Photochemistry and Photobiology*, *62*, 17–23.

Boukhalfa-Heniche, F. Z., Hernández, B., Gaillard, S., Coïc, Y. M., Huynh-Dinh, T., Lecouvey, M., et al. (2004). Complex formation and vectorization of a phosphorothioate oligonucleotide with an amphipathic leucine- and lysine-rich peptide: Study at molecular and cellular levels. *Biopolymers*, *73*, 727–734.

Bour, P., Kim, J., Kapitan, J., Hammer, R. P., Huang, R., Wu, L., et al. (2008). Vibrational circular dichroism and IR spectral analysis as a test of theoretical conformational modelling for a cyclic hexapeptide. *Chirality*, *20*, 1104–1119.

Brabander, T., van der Zwan, W. A., Teunissen, J. J., Kam, B. L., Feelders, R. A., de Herder, W. W., et al. (2017). Long-term efficacy, survival and safety of [^{177}Lu-DOTA^{0}, Tyr^{3}]octreotate in patients with gastroenteropancreatic and bronchial neuroendocrine tumors. *Clinical Cancer Research*, *23*, 4617–4624.

Brazeau, P., Vale, W., Burgus, R., Ling, N., Butcher, M., Rivier, J., et al. (1973). Hypothalamic polypeptide that inhibits the secretion of immunoreactive pituitary growth hormone. *Science*, *179*, 77–79.

Brown, M., Rivier, J., & Vale, W. (1976). Biological activity of somatostatin and somatostatin analogs on inhibition of arginine-induced insulin and glucagon release in the rat. *Endocrinology*, *98*, 336–343.

Bruns, C., Lewis, I., Briner, U., Meno-Tetang, G., & Weckbecker, G. (2002). SOM230: A novel Somatostatin peptidomimetic with broad somatotropin release inhibiting factor (SRIF) receptor binding and a unique antisecretory profile. *European Journal of Endocrinology*, *146*, 707–716.

Cañamares, M. V., Garcia-Ramos, J. V., Gómez-Varga, J. D., Domingo, C., & Sanchez-Cortes, S. (2005). Comparative study of the morphology, aggregation, adherence to

glass, and surface-enhanced Raman scattering activity of silver nanoparticles prepared by chemical reduction of Ag^{+} using citrate and hydroxylamine. *Langmuir*, *21*, 8546–8553.
Caplin, M. E., Pavel, M., Cwikla, J. B., Phan, A. T., Raderer, M., Sedláčková, E., et al. (2014). Lanreotide in metastatic enteropancreatic neuroendocrine tumors. *The New England Journal of Medicine*, *371*, 224–233.
Casals, E., Pfaller, T., Duschl, A., Oostingh, G. J., & Puntes, V. (2010). Time evolution of the nanoparticle protein corona. *ACS Nano*, *4*, 3623–3632.
Chatalic, K. L., Kwekkeboom, D. J., & de Jong, M. (2015). Radiopeptides for imaging and therapy: A radiant future. *Journal of Nuclear Medicine*, *56*, 1809–1812.
Chen, J., Ding, W., Luo, Z., Loo, B. H., & Yao, J. (2015). Probing single molecules and molecular aggregates: Raman spectroscopic advances. *Journal of Raman Spectroscopy*, *47*, 623–635.
Das, C., Naganagowda, G. A., Karle, I. L., & Balaram, P. (2001). Designed beta-hairpin peptides with defined tight turn stereochemistry. *Biopolymers*, *58*, 335–346.
Fuchs, P. F., Bonvin, A. M., Bochicchio, B., Pepe, A., Alix, A. J., & Tamburro, A. M. (2006). Kinetics and thermodynamics of type VIII beta-turn formation: A CD, NMR, and microsecond explicit molecular dynamics study of the GDNP tetrapeptide. *Biophysical Journal*, *90*, 2745–2759.
Garrell, R. L., Shaw, K. D., & Krimm, S. (1983). Surface enhanced Raman spectroscopy of halide ions on colloidal silver: Morphology and coverage. *Surface Science*, *124*, 613–624.
Gibbs, A. C., Bjorndahi, T. C., Hodges, R. S., & Wishart, D. S. (2002). Probing the structural determinants of type II' beta-turn formation in peptides and proteins. *Journal of the American Chemical Society*, *124*, 1203–1213.
Guerrini, L., Izquierdo-Lorenzo, I., Garcia-Ramos, J. V., Domingo, C., & Sanchez-Cortes, S. (2009). Self-assembly of α,ω-aliphatic diamines on Ag nanoparticles as an effective localized surface plasmon nanosensor based in interparticle hot spots. *Physical Chemistry Chemical Physics*, *11*, 7363–7371.
Guiffo-Soh, G., Hernández, B., Coïc, Y. M., Boukhalfa-Heniche, F. Z., Fadda, G., & Ghomi, M. (2008). Vibrational analysis of amino acids and short peptides in hydrated media. 3. Successive KL repeats induce highly stable beta-strands capable of forming non-H-bonded aggregates. *The Journal of Physical Chemistry B*, *112*, 1282–1289.
Guiffo-Soh, G., Hernández, B., Coïc, Y. M., Boukhalfa-Heniche, F. Z., & Ghomi, M. (2007). Vibrational analysis of amino acids and short peptides in hydrated media. II. Role of KLLL repeats to induce helical conformations in minimalist LK-peptides. *The Journal of Physical Chemistry B*, *111*, 12563–12572.
Gunasekaran, K., Ramakrishnan, C., & Balaram, P. (1997). Beta-hairpins in proteins revisited: Lessons for de novo design. *Protein Engineering*, *10*, 1131–1141.
Hallenga, K., van Binst, G., Knappenberg, M., Brison, J., Michel, A., & Dirkx, J. (1979). The conformational properties of some fragments of the peptide hormone somatostatin. *Biochimica et Biophysica Acta*, *577*, 82–101.
Hallenga, K., van Binst, G., Scarso, A., Michel, A., Knappenberg, M., Dremier, C., et al. (1980). The conformational properties of the peptide hormone somatostatin (III). Assignment and analysis of the ^{1}H and ^{13}C high resolution NMR spectra of somatostatin in aqueous solution. *FEBS Letters*, *119*, 47–52.
Hernández, B., Boukhalfa-Heniche, F. Z., Seksek, O., Coïc, Y. M., & Ghomi, M. (2006). Secondary conformation of short lysine- and leucine-rich peptides assessed by optical spectroscopies: Effect of chain length, concentration, solvent, and time. *Biopolymers*, *81*, 8–19.
Hernández, B., Carelli, C., Coïc, Y. M., De Conninck, J., & Ghomi, M. (2009). Vibrational analysis of amino acids and short peptides in aqueous media. V. The effect of the disulfide bridge on the structural features of the peptide hormone somatostatin-14. *The Journal of Physical Chemistry B*, *113*, 12796–12803.

Hernández, B., Coïc, Y. M., Baron, B., Kruglik, S. G., Pflüger, F., Cohen, R., et al. (2014). Low concentration structural dynamics of lanreotide and somatostatin-14. *Biopolymers*, *101*, 1019–1028.

Hernández, B., Coïc, Y. M., Gouyette, C., & Ghomi, M. (2012). Probing the interactions of oligodeoxynucleotides with a cationic peptide by Raman scattering. In M. Ghomi (Ed.), *Applications of Raman spectroscopy to biology. From basic studies to disease diagnosis* (pp. 58–71). Amsterdam, The Netherlands: IOS Press.

Hernández, B., Coïc, Y. M., Kruglik, S. G., Carelli, C., Cohen, R., & Ghomi, M. (2012). Octreotide used for probing the type-II′ β-turn CD and Raman markers. *The Journal of Physical Chemistry B*, *116*, 9337–9345.

Hernández, B., Coïc, Y. M., Pflüger, F., Kruglik, S. G., & Ghomi, M. (2015). All characteristic Raman markers of tyrosine and tyrosinate originate from phenol ring fundamental vibrations. *Journal of Raman Spectroscopy*, *47*, 210–220.

Hernández, B., López-Tobar, E., Sanchez-Cortes, S., Coïc, Y. M., Baron, B., Chenal, A., et al. (2016). From bulk to plasmonic nanoparticle surfaces: The behaviour of two potent therapeutic peptides, octreotide and pasireotide. *Physical Chemistry Chemical Physics*, *18*, 24437–24450.

Hernández, B., Pflüger, F., Adenier, A., Kruglik, S. G., & Ghomi, M. (2010). Vibrational analysis of amino acids and short peptides in hydrated media. VIII. Amino acids with aromatic side chains: L-phenylalanine, L-tyrosine, and L-tryptophan. *The Journal of Physical Chemistry B*, *114*, 15319–15330.

Hernández, B., Pflüger, F., Kruglik, S. G., & Ghomi, M. (2013). Characteristic Raman lines of phenylalanine analyzed by a multiconformational analysis. *Journal of Raman Spectroscopy*, *44*, 827–833.

Hernández, B., Pflüger, F., López-Tobar, E., Kruglik, S. G., Garcia-Ramos, J. V., Sanchez-Cortes, S., et al. (2014). Disulfide linkage Raman markers: A reconsideration attempt. *Journal of Raman Spectroscopy*, *45*, 657–664.

Hogg, P. J. (2013). Targeting allosteric disulphide bonds in cancer. *Nature Reviews. Cancer*, *13*, 425–431.

Holladay, L. A., & Puett, D. (1976). Somatostatin conformation: Evidence for a stable intramolecular structure from circular dichroism, diffusion, and sedimentation equilibrium. *Proceedings of the National Academy of Sciences of the United States of America*, *73*, 1199–1202.

Holladay, L. A., Rivier, J., & Puett, D. (1977). Conformational studies on somatostatin and analogues. *Biochemistry*, *16*, 4895–4900.

Hsieh, H., Chang, C. W., & Cho, H. H. (2013). Gold nanoparticles as amyloid fibrillogenesis inhibitors. *Colloids and Surfaces, B: Biointerfaces*, *112*, 525–529.

Huang, X., El-Sayed, I. H., Qian, W., & El-Sayed, M. A. (2006). Cancer cell imaging and photothermal therapy in the near-infrared region by using gold nanorods. *Journal of the American Chemical Society*, *128*, 2115–2120.

Hutter, E., & Fendler, J. H. (2004). Exploitation of localized surface plasmon resonance. *Advanced Materials*, *16*, 1685–1706.

Interlandi, G. (2009). Backbone conformations and side chain flexibility of two somatostatin mimics investigated by molecular dynamics simulations. *Proteins*, *75*, 659–670.

Jain, P. K., El-Sayed, I. H., & El-Sayed, M. A. (2007). Au nanoparticles target cancer. *Nano Today*, *2*, 18–29.

Jiménez-Mancilla, N., Ferro-Flores, G., Santos-Cuevas, C., Ocampo-García, B., Luna-Gutiérrez, M., Azorin-Vega, E., et al. (2013). Multifunctional targeted therapy system based on ^{99m}Tc/^{177}Lu-labeled gold nanoparticles-Tat(49–57)-Lys^3-bombesin internalized in nuclei of prostate cancer cells. *Journal of Labelled Compounds and Radiopharmaceuticals*, *56*, 663–671.

Karimi, M., Zare, H., Bakhshian Nik, A., Yazdani, N., Hamrang, M., Mohamed, E., et al. (2016). Nanotechnology in diagnosis and treatment of coronary artery disease. *Nanomedicine*, *11*, 513–530.

Kaur, H., & Raghava, G. P. S. (2004). A neural network method for prediction of β-turn types in proteins using evolutionary information. *Bioinformatics*, *20*, 2751–2758.
Kelly, S. M., & Price, N. C. (2000). The use of circular dichroism in the investigation of protein structure and function. *Current Protein & Peptide Science*, *1*, 349–384.
Khan, S., Gupta, A., & Nandi, C. K. (2013). Controlling the fate of protein corona by tuning surface properties of nanoparticles. *Journal of Physical Chemistry Letters*, *4*, 3747–3752.
Kharlamov, A. N., Tyurnina, A. E., Veselova, V. S., Kovtun, O. P., Shur, V. Y., & Gabinsky, J. L. (2015). Silica-gold nanoparticles for atheroprotective management of plaques: Results of the NANOM-FIM trial. *Nanoscale*, 7, 8003–8015.
Knappenberg, M., Michel, A., Scarso, A., Brison, J., Zanen, J., Hallenga, K., et al. (1982). The conformational properties of somatostatin. IV. The conformers contributing to the conformation equilibrium of somatostatin in aqueous solution as found by semi-empirical energy calculations and high-resolution NMR experiments. *Biochimica et Biophysica Acta*, *18*, 229–246.
Lackowicz, J. R., Principles of fluorescence spectroscopy (2006). (3rd ed.). New York: Springer.
Lazo, N. D., & Downing, D. T. (2001). Effects of Na_2SO_4 on hydrophobic and electrostatic interactions between amphipathic α-helices. *The Journal of Peptide Research*, *58*, 457–463.
Lee, K. S., & El-Sayed, M. A. (2006). Gold and silver nanoparticles in sensing and imaging: Sensitivity of plasmon response to size, shape, and metal composition. *The Journal of Physical Chemistry. B*, *110*, 19220–19225.
Lewis, L., Albert, R., Bauer, W., Chandramouli, N., Pless, J., Oberer, L., et al. (2004). The superior therapeutic properties of SOM230 originate from unique structural elements. *CHIMIA*, *58*, 222–227.
Li, Y., Jing, C., Zhang, L., & Long, Y. T. (2012). Resonance scattering particles as biological nanosensors *in vitro* and *in vivo*. *Chemical Society Reviews*, *41*, 632–642.
Linse, S., Cabaleiro-Lago, C., Xue, W. F., Lynch, I., Lindman, S., Thulin, E., et al. (2007). Nucleation of protein fibrillation by nanoparticles. *Proceedings of the National Academy of Sciences of the United States of America*, *104*, 8691–8696.
Liz-Marzán, L. M. (2004). Nanometals formation and color. *Materials Today*, 7, 26–31.
López-Tobar, E., Hernández, B., Ghomi, M., Gómez, J., Chenal, A., Garcia Ramos, J. V., et al. (2015). Anchoring sites of fibrillogenic peptide hormone somatostatin-14 on plasmonic nanoparticles. *Journal of Physical Chemistry C*, *119*, 8273–8279.
López-Tobar, E., Hernández, B., Ghomi, M., & Sanchez-Cortes, S. (2013). Stability of the disulfide bond in cystine adsorbed on silver and gold nanoparticles as evidenced by SERS data. *Journal of Physical Chemistry C*, *117*, 1531–1537.
Ma, Q., Wei, G., & Yang, X. (2013). Influence of Au nanoparticles on the aggregation of amyloid-β-(25 − 35) peptides. *Nanoscale*, *5*, 10397–10403.
Mahalakshimi, R., Shanmugam, G., Polavarapu, P. L., & Balaram, P. (2005). Circular dichroism of designed peptide helices and β-hairpins: Analysis of Trp- and Tyr-rich peptides. *Chembiochem*, *6*, 2152–2158.
Maji, S. K., Perrin, M. H., Sawaya, M. R., Jessberger, S., Vadodaria, K., Rissman, R. A., et al. (2009). Functional amyloids as natural storage of peptide hormones in pituitary secretory granules. *Science*, *325*, 328–332.
McKeage, K. (2013). Pasireotide: A review of its use in Cushing's disease. *Drugs*, *73*, 563–574.
Melacini, G., Zhu, Q., & Goodman, M. (1997). Multiconformational NMR analysis of sandostatin (octreotide): Equilibrium between beta-sheet and partially helical structures. *Biochemistry*, *36*, 1233–1241.

Mendoza-Nava, H., Ferro-Flores, G., Ocampo-García, B., Serment-Guerrero, J., Santos-Cuevas, C., Jiménez-Mancilla, N., et al. (2013). Laser heating of gold nanospheres functionalized with octreotide: In vitro effect on HeLa cell viability. *Photomedicine and Laser Surgery*, *31*, 17–22.

Merola, E., Panzuto, F., & Delle Fave, G. (2017). Antiproliferative effect of somatostatin analogs in advanced gastro-entero-pancreatic neuroendocrine tumors: A systematic review and meta-analysis. *Oncotarget*, *8*, 46624–46634.

Milner-White, E. J., Ross, B. M., Ismail, R., Belhadj-Mostefa, K., & Poet, R. (1988). One type of gamma-turn, rather than the other gives rise to chain-reversal in proteins. *Journal of Molecular Biology*, *204*, 777–782.

Modlin, I. M., Pavel, M., Kidd, M., & Gustafsson, B. I. (2010). Somatostatin analogues in the treatment of gastroenteropancreatic neuroendocrine (carcinoid) tumours. *Alimentary Pharmacology & Therapeutics*, *31*, 169–188.

Mohamed, A., Blanchard, M. P., Albertelli, M., Barbieri, F., Brue, T., Niccoli, P., et al. (2014). Pasireotide and octreotide antiproliferative effects and sst2 trafficking in human pancreatic neuroendocrine tumor cultures. *Endocrine-Related Cancer*, *21*, 691–704.

Motta, A., Reches, M. R., Pappalardo, L., Andretti, G., & Gazit, E. (2005). The preferred conformation of tripeptide Ala-Phe-Ala in water is an inverse γ-turn: Implications for protein folding and drug design. *Biochemistry*, *44*, 14170–14178.

Nergiz, S. Z., Slocik, J. M., Naik, R. R., & Singamaneni, S. (2013). Surface defect sites facilitate fibrillation: An insight into adsorption of gold-binding peptides on Au (111). *Physical Chemistry Chemical Physics*, *15*, 11629–11633.

Nima, Z. A., Alwbari, A. M., Dantuluri, V., Hamzah, R. N., Sra, N., Motwani, P., et al. (2017). Targeting nano drug delivery to cancer cells using tunable, multi-layer, silver-decorated gold nanorods. *Journal of Applied Toxicology*, *37*, 1370–1378.

Otting, G., Liepinsh, E., & Wüthrich, K. (1991). Protein hydration in aqueous solution. *Science*, *254*, 974–980.

Paige Hall, W., Anker, J. N., Lin, Y., Modica, J., Mrksich, M., & van Duyne, R. P. (2008). A calcium-modulated plasmon switch. *Journal of the American Chemical Society*, *130*, 5836–5837.

Pawlikowski, M., & Meleń-Mucha, G. (2004). Somatostatin analogs—From new molecules to new applications. *Current Opinion in Pharmacology*, *4*, 608–613.

Pelaz, B., del Pino, P., Maffre, P., Hartmann, R., Gallego, M., Rivera-Fernández, S., et al. (2015). Surface functionalization of nanoparticles with polyethyleneglycol: Effects on protein adsorption and cellular uptake. *ACS Nano*, *9*, 6996–7008.

Perczel, A., & Fasman, G. D. (1992). Quantitative analysis of cyclic beta-turn models. *Protein Science*, *1*, 378–395.

Pohl, E., Heine, A., Sheldrick, G. M., Dauter, Z., Wilson, K. S., Kallen, J., et al. (1995). Structure of octreotide, a somatostatin analogue. *Acta Crystallographica*, *D51*, 48–59.

Qian, R., Cao, Y., & Long, Y. T. (2016). Dual-targeting nanovesicles for in situ intracellular imaging of and discrimination between wild-type and mutant p53. *Angewandte Chemie International Edition*, *55*, 719–723.

Reubi, J., Waser, B., Schaer, J. C., & Laissue, J. A. (2001). Somatostatin receptor sst1–sst5 expression in normal and neoplastic human tissues using receptor autoradiography with subtype-selective ligands. *European Journal of Nuclear Medicine*, *28*, 836–846.

Rinke, A., Muller, H. H., Schade-Brittinger, C., Klose, K. J., Barth, P., Wied, M., et al. (2009). Placebo controlled, double-blind, prospective, randomized study on the effect of octreotide LAR in the control of tumor growth in patients with metastatic neuroendocrine midgut tumors: A report from the PROMID Study Group. *Journal of Clinical Oncology*, *27*, 4656–4663.

Sanchez-Cortes, S., Garcia-Ramos, J. V., Morcillo, G., & Tinti, A. (1995). Morphological study of silver colloids employed in surface- enhanced Raman spectroscopy: Activation when exciting in visible and near-infrared regions. *Journal of Colloid and Interface Science*, *175*, 358–368.

Schmidt, B., Ho, L., & Hogg, P. J. (2006). Allosteric disulfide bonds. *Biochemistry*, *45*, 7429–7433.

Schmidt, B., & Hogg, P. J. (2007). Search for allosteric disulfide bonds in NMR structures. *BMC Structural Biology*, *7*, 49.

Sevilla, P., Lajos, G., de Llanos, R., Sanchez-Cortes, S., Jancura, D., Miškovský, P., et al. (2012). Surface-enhanced fluorescence and Raman spectroscopy (SEF and SERS) of anthraquinone anti tumoral drugs and their complex with biomolecules on Ag nanoparticles. In M. Ghomi (Ed.), *Applications of Raman spectroscopy to biology*. *From basic studies to disease diagnosis* (pp. 31–57). Amsterdam, The Netherlands: IOS Press.

Shekhter Zahavi, T., Oron-Herman, M., Kostenich, G., Rub, E., Salitra, Y., Buzhansky, L., et al. (2017). Molecular engineering of somatostatin analogue with minimal dipeptide motif induces the formation of functional nanoparticles. *ChemNanoMat*, *3*, 27–32.

Shenashen, M. A., El-Safty, S. A., & Elshehy, E. A. (2013). Synthesis, morphological, and properties of silver nanoparticles in potential applications. *Particle and Particle Systems Characterization*, *31*, 293–316.

Sibanda, B. L., & Thornton, J. M. (1985). β-Hairpin families in globular proteins. *Nature*, *316*, 170–174.

Skaat, H., Shafir, G., & Margel, S. (2011). Acceleration of amyloid-β fibril formation by peptide-conjugated fluorescent-maghemite nanoparticles. *Journal of Nanoparticle Research*, *13*, 3521–3534.

Sugeta, H., Go, A., & Miyazawa, T. (1972). S-S and C-S stretching vibrations and molecular conformations of dialkyl disulfides and cystine. *Chemistry Letters*, *1*, 83–86.

Vale, W., Grant, G., Amoss, M., Blackwell, R., & Guillemin, R. (1972). Culture of enzymatically dispersed pituitary cells: Functional validation of a method. *Endocrinology*, *91*, 562–572.

van Grondelle, W., Lecomte, S., Lopez-Iglesias, C., Manero, J. M., Cherif-Cheikh, R., Paternostre, M., et al. (2013). Lamination and spherulite-like compaction of a hormone's native amyloid-like nanofibrils: Spectroscopic insights into key interactions. *Faraday Discussions*, *166*, 163–180.

van Grondelle, W., Lopez-Iglesias, C., Coll, E., Artzner, F., Paternostre, M., Lacombe, F., et al. (2007). Spontaneous fibrillation of the native neuropeptide hormone Somatostatin-14. *Journal of Structural Biology*, *160*, 211–213.

Van Wart, H. E., & Scheraga, H. A. (1976). Raman spectra of strained disulfides. Effect of rotation about sulfur-sulfur bonds on sulfur-sulfur stretching frequencies. *The Journal of Physical Chemistry*, *80*, 1823–1832.

Van Wart, H. E., & Scheraga, H. A. (1986). Agreement with the disulfide stretching frequency-conformation correlation of Sugeta, Go, and Miyazawa. *Proceedings of the National Academy of Sciences of the United States of America*, *83*, 3064–3067.

Walkey, C. D., Olsen, J. B., Song, F., Liu, R., Guo, H., Olsen, D. W. H., et al. (2014). Protein corona fingerprinting predicts the cellular interaction of gold and silver nanoparticles. *ACS Nano*, *8*, 2439–2455.

Wang, L., Tang, K., Zhang, Q., Li, H., Wen, Z., Zhang, H., et al. (2013). Somatostatin receptor-based molecular imaging and therapy for neuroendocrine tumors. *BioMed Research International*, *2013*, 102819.

Weckbecker, G., Lewis, I., Albert, R., Schmid, H. A., Hoyer, D., & Bruns, C. (2003). Opportunities in somatostatin research: Biological, chemical and therapeutic aspects. *Nature Reviews. Drug Discovery*, *2*, 999–1017.

Yao, J. C., Hassan, M., Phan, A., Dagohoy, C., Leary, C., Mares, J. E., et al. (2008). One hundred years after "carcinoid": Epidemiology of and prognostic factors for neuroendocrine tumors in 35,825 cases in the United States. *Journal of Clinical Oncology*, *26*, 3063–3072.

Yoo, S. I., Yang, M., Brender, J. R., Subramanian, V., Sun, K., Joo, N. E., et al. (2011). Inhibition of amyloid peptide fibrillation by inorganic nanoparticle: Functional similarities with proteins. *Angewandte Chemie*, *50*, 5110–5115.

Zhong, D., Pal, S. K., & Zewail, A. H. (2011). Biological water: A critique. *Chemical Physics Letters*, *503*, 1–11.